1. AGENCY USE ONLY (Leave Blank)	2. REPORT DATE	3. REPORT TYPE AND DATES COVERED Final Technical Report 6/99-12/31/03

4. TITLE AND SUBTITLE Compact Reconfigurable High Frequency-Ultrahigh Frequency (HG-UHF) Antenna	5. FUNDING NUMBERS DAAD19-99-1-0197

6. AUTHOR(S)

Kamal Sarabandi, Ph.D.

7. PERFORMING ORGANIZATION NAME(S) AND ADDRESS(ES) The University of Michigan, Department of EECS 1301 Beal Avenue, Room 3228B Ann Arbor, MI 48109-2122	8. PERFORMING ORGANIZATION REPORT NUMBER

9. SPONSORING / MONITORING AGENCY NAME(S) AND ADDRESS(ES) U. S. Army Research Office P.O. Box 12211 Research Triangle Park, NC 27709-2211	10. SPONSORING / MONITORING AGENCY REPORT NUMBER 39879.1-EL

11. SUPPLEMENTARY NOTES

The views, opinions and/or findings contained in this report are those of the author(s) and should not be construed as an official Department of the Army position, policy or decision, unless so designated by other documentation.

12 a. DISTRIBUTION / AVAILABILITY STATEMENT Approved for public release; distribution unlimited.	12 b. DISTRIBUTION CODE

13. ABSTRACT (Maximum 200 words)

The goal of this research effort was the development of computer algorithms for the predication of radio wave propagation in forest or Vegetated environments. In addition, recognizing the need for measured data sets for validation of such modesl, two measurements Campaigns were conducted, one to determine path loss for near-Earth propagation and one which utilizes a unique, synchronized, long-range measurement system (the system has been tested to over a kilometer, and in principle will work over longer ranges), developed for this project, and which allos for the evaluation of both pathloss and frequency decorrelation. Since the start of the project in May, 2001, significant progress was made towards achieving the project goal. A physics-based methodology was used, in which the actual physical scenario of a given propagation problem or environment is modeled. A description of this physics-based methodology and why this approach is applied is given in the final technical report. The impact of this effort on FCS and related programs is then discussed, followed by a brief summary of the project accomplishments. Completed work is then described. Where noted, expanded and detailed discussions of several of the developed algorithms is later given.

14. SUBJECT TERMS	15. NUMBER OF PAGES
	16. PRICE CODE

17. SECURITY CLASSIFICATION OR REPORT UNCLASSIFIED	18. SECURITY CLASSIFICATION ON THIS PAGE UNCLASSIFIED	19. SECURITY CLASSIFICATION OF ABSTRACT UNCLASSIFIED	20. LIMITATION OF ABSTRACT UL

DARPA-FCS Final Report

The University of Michigan's Radiation Laboratory

Department of Electrical Engineering & Computer Science

1301 Beal Avenue

Ann Arbor, Michigan 48109-2122

Contact: Professor Kamal Sarabandi

Phone: (734) 936-1575

Fax: (734) 647-2106

email: saraband@eecs.umich.edu

Contents

1 Executive Summary

Participants

Principle Investigator:
Professor Kamal Sarabandi

Research Scientists and Fellows:
Mark D. Casciato, Il-Suek Koh, Adib Nashashibi, and Leland Pierce

Graduate Students:
Farshid Aryanfar, Nader Behdad, and Feinian Wang

bf Technical Staff:
Adam Hartz, Brett Lyons, and Wayne Walker

1.1 Wave Propagation in Foliage: Overview and Project Goals

Significant progress has been made in the development of a set of simulation tools for the prediction of channel effects on a radio signal propagating in a forest or vegetated environment, as well as in developing measurement techniques and systems for validating such tools. Complex and rigorous mathematical formulations have been developed and combined with efficient computer algorithms to produce a set of simulations tools which characterize and predict channel effects to a degree of accuracy and generality not previously available.

To date no general tools are available to system design engineers, which would give them the ability to accurately assess the performance of a complex communication system and evaluate the channel capacity. An accurate and general model of the propagation channel is critical for evaluating system performance in terms of system parameters such as the trade-off between radiated power and signal processing, modulation schemes, diversity schemes, etc., and such a tool would give the system engineer a-priori knowledge of optimum system configuration, without the need for costly prototypes.

Having recognized this deficiency, the goal of this research effort was the development of computer algorithms for the prediction of radio wave propagation in forest or vegetated environments. In addition, recognizing the need for measured data sets for validation of such models, two measurements campaigns were conducted, one to determine path loss for near-Earth propagation and one which utilizes a unique, synchronized, long-range measurement system (the system has been tested to over a kilometer, and in principle will work over longer ranges), developed for this project, and which allows for the evaluation of both pathloss and frequency decorrelation. Since the start of the project in May 2001, significant progress was made towards achieving the project goal. A physics-based methodology was used, in which the actual physical scenario of a given propagation problem or environment is modeled. A description of this physics-based methodology and why this approach is applied is given next. The impact of this effort on FCS and related programs is then discussed, followed by a brief summary of the project accomplishments. Completed work is then described. Where noted, expanded and detailed discussions of several of the developed algorithms is later given.

1.2   Methodology: A Physics-based Approach

Accurate estimation of channel response requires a high fidelity model that preserves the physics of wave interaction with scatterers and objects within the channel. At the heart of this channel model must be a set of physics-based models obtained from a rigorous application of electromagnetic wave theory applied to a number of physical scenarios pertinent to the propagation environment.The basic approach is to develop a series of canonical models representing various possible features in the environment which effect the radio wave. For example tree trunks are modeled as layered dielectric cylinders, leaves on deciduous trees as flat, oblong resistive sheets, needles on coniferous trees as very small dielectric cylinders, the Earth, locally, as a flat impedance sheet. The appropriate method, whether analytic, numeric, or some hybrid method, is applied to solve the electromagnetic scattering/diffraction problem, with approximations made which maximize the efficiency of the simulation in terms of computer resources while at the same time retaining the desired degree of accuracy. The eventual goal is to combine these canonical models in the appropriate fashion for a site-specific propagation simulation tool. For example, for a specific tree stand a mathematical model (fractal) in conjunction with botanical information is used to construct a realistic forest stand. The parameters of the scene, such as topography, land use, etc., can be determined from a satellite data base. A wideband, Monte Carlo simulation is then applied, which provides accurate data from which the received field statistics, path loss, dispersive effects (multipath), and impulse response can be determined.

1.3   Why A Physics-based Approach

Traditionally, there are several methods applied for predicting the effects of the channel, in a communications system. These methods can be divided into two basic technique, measurement based models, and simple theoretical models. Both techniques have significant shortcomings which are discussed in the following.

1.3.1   Measurement Based Channel Models

In this heuristic approach measured data is analyzed and the data fitted to a statistical curve. The basic problem with this approach is that the measured data is very specific to the measurement setup and measured environment. In addition, measured data exists only for specific frequency bands and for some desired channel parameter such as path loss which cannot be easily extrapolated. Basically the time and cost required to extend this data base to account for a more complete propagation scenario is quite simply put, impossible.

1.3.2   Basic Theoretical Models

In this approach basic electromagnetic theory is applied to the propagation problem, albeit in its simplest form. The rigorous application of electromagnetic wave theory (i.e., a description of the actual physics involved) is not trivial. In these basic models, assumptions are made which while significantly simplifying the problem, also make the resulting formulations limited in accuracy and as the approximations made tend to distance the resulting formulations from the physics of the problem, they are limited in generality.

1.4   Impact on FCS and Related Programs

- The accurate channel simulation tool being developed will allow the FCS participants to examine, refine, and optimize the wireless system under development.

- These include, (but are not limited to):

    Ad-hoc network of communication systems over a frequency range from HF through Ka-band.

    An unattended network of sensors.

    Microwave and millimeter-wave radar detection of objects concealed in foliage.

- The foliage models are being integrated into TIREM in order to expand upon its capabilities to account for the effects of vegetation in a more accurate and general fashion.

1.5   Brief Summary of Accomplishments

1.5.1   Data Generation

- Data Generation: Data was generated for coniferous trees from 200 MHz to 3 GHz at two receiver heights (1.5 and 3 m). The original C code was ported to FORTRAN for increased faster run-times, and this and other improvements in code efficiency, allowed for the complete data set, at both receiver heights, to be generated in 3 weeks, a task that would have taken several years before the code improvements were made. Separation of the received field into direct and reflected components allowed for minimal sampling in the frequency domain, thus further improving the code run-time, while still capturing the oscillatory pattern, as a function of frequency, in the total received fields. Coefficients for the functional form of this data set were generated and sent to Steve Fast and George Liang (at Penn State and EMAG technologies, respectively).

1.5.2   Code Improvement & Algorithm Development

Additional progress has been made in development electromagnetic (EM) algorithms to improve code accuracy and efficiency at both low and high frequencies.

- **MoM for Coniferous Needles at mm-wave:** Multiple scattering between coniferous needles has a significant effect on the received field. The large number of needles on coniferous trees results in a significant slow-down in code run-time at all frequencies, but at mm-wave frequencies, where all features of a tree are electrical large, the problem can be intractable, even for analytic solutions which do not account for the multiple scattering effect, and are thus inaccurate. Because of these problems, an alternate, accurate, and computationally efficient method is sought, which accounts for the multiple scattering effect. Work was begun on development of a more efficient computational algorithm to handle the EM scattering from needles, by applying a numerical technique known as Method of Moments (MoM). MoM involves inversion of a large matrix (Z-matrix) and standard MoM techniques can also be computationally intensive, but the modified MoM applied here exploits the independence of the Z-matrix on the incident field and results in a more computationally tractable problem. Details of this work can be found in Section 2.

- **FMM Technique for Improved Computational Efficiency:** For calculating the interaction between tree structures using MoM the problem can be made more tractable by applying an approximate technique known as the Fast Multipole Method (FMM). MoM is an integral equation technique which applies a complex Green's function and computes the interaction between cells of the computational domain. By taking into account the relative distance between scattering centers, FMM calculates an approximate far-field Green's function, which is computationally faster, for calculation of this interaction. Unlike existing approximate formulations this new multipole representation of the Green's function for the half-space impedance surface problem does not impose any restrictions on the location of source or observation points and is computationally very efficient. Section 3 gives details and results of the new method.

1.5.3 Generation and Visualization of the Physical Environment

Progress also has been made on this project in the generation and visualization of the physical propagation scenario, mainly for forested environments, but additional work has also been done in order to generate other features found in a propagation environment, such as buildings and structures. Completed work includes creation of a scale model of the Lakehurst Naval Air Station for use by an EM simulator which uses a ray-tracing method. Figure 1 shows a graphical rendition of the Lake Hurst site.
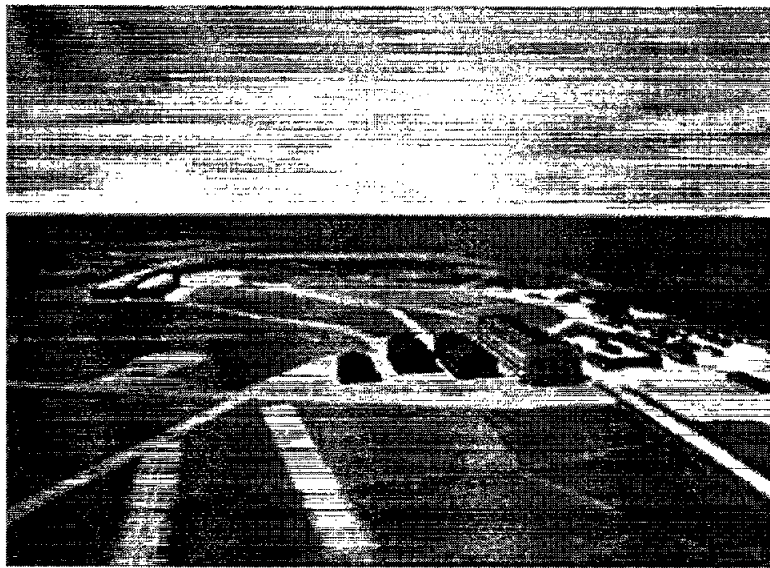
Figure 1: Graphical Rendition of the Lakehurst Naval Air Station

1.5.4 Rural and Urban Propagation Simulator

An important development in this project is the integration of the previously discussed scene generator with an electromagnetic simulator, which uses a fast ray-tracing algorithm to simulate propagation in both rural and urban environments. Completed work includes path loss prediction on a mobile platform in an urban environment (a computer recreation of downtown Ann Arbor, Michigan) and as mentioned creation of a scale model of the Lakehurst Navel Air Station for use by the ray-tracing simulation. Details and results of the ray-tracing simulation will be shown in Section 4.

1.5.5 Near-surface Propagation Measurements in Forest and Grassy Areas from 400 MHz to 35 GHz

A set of outdoor measurements was conducted in both a deciduous forest, and a more open grassy area. The intent of this measurement was to was to gain some initial insight into the phenomenology of propagation in forested environments, when both transmitter and receiver are in close proximity to the Earth. Measurement results indicate that the phenomenon of radio wave propagation is very site specific and both details of the propagation scenario as well as accurate EM models are necessary for accurate simulations. Details of this measurement campaign are given in Section 5.

1.5.6 A Measurement System for Ultra Wideband Communication Channel Characterization

As part of a continuing effort to evaluate the accuracy of channel models, a novel, wideband propagation channel measurement system was developed and the system tested in a measurements campaign at the Lakehurst Naval Air Station, in Lakehurst, NJ. The developed system is unique, and can provide the end user with complete information on the effects of forest and vegetation. Measurements were be made over a frequency range from 30MHz to 3GHz.

In a manner similar to a bi-static radar measurement, the experimental set-up consists of a low-noise receiver, time synchronized with a high-power transmitter (using HP network analyzers to both transmit and receive). Time synchronization is carried out by using a pair of rubidium atomic clocks, and GPS receivers. The sliding, narrow-band filter of the network analyzer frequency sweep maximizes receiver sensitivity, necessary over the long transmitter paths involved (over 1km). Time synchronization of the transmitter and receiver allows for a fully coherent measurement system, providing unique information on propagation and path loss to the end user.

The system enables the user to characterize signal propagation through a medium over a very wide frequency band with fine spectral resolution (as low as 3 Hz) by measuring the attenuation and phase characteristics of the medium. This system also allows for the study of temporal, spectral and spatial decorrelation. The high fidelity data gathered with this system can also be utilized to develop empirical models or used as a validation tool for physics based propagation models. The mobility and flexibility of the system allows for site specific measurements in various propagation scenarios. Details of this system, as well as results from the Lakehurst measurements campaign are shown in Section 6.

2 Scattering from a Pine Needle Cluster using Method of Moments (MoM)

2.1 Introduction

A pine needle cluster is composed of a number of pine needles growing on a single stem. Both the stem and the needles can be modeled as dielectric cylinders of finite length. The solution to scattering from a finite cylinder is known [1], and from this a formulation to model the scattering from an entire needle cluster has also been developed [2]. However, this method is limited in that the effect of coupling between individual needles is neglected.

An example of a pine needle cluster is shown in Figure 2, where the location of the pine needles are distributed as a spiral and the tilt angle of the needles (angle from the stem axis, z-axis in Figure 2) decreases as they approach the tip of the stem. The minimum distance between each pair of needles is about 5 mm, less than one wavelength at mm-wave frequencies. In this case, geometric optics (GO) is not suitable to accurately model the coupling between needles. Numerical methods, such as FEM (Finite Element Method) and MOM (Method of Moment), are better choices, however unlike FEM MoM only requires that the scatterer itself be defined in the computational domain, which is more conducive to free geometries such as a needle cluster, and therefore Mom will be applied in this investigation.
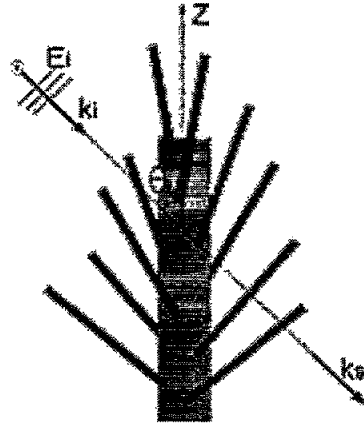
Figure 2: A pine needle cluster model.

2.2 MOM Formulation

For this MoM formulation pulse basis functions (constant current across each cell is assumed) and point matching for weighting functions, along with the volume equivalence principle are applied, as in [1] for a single needle (for the time being, the stem is excluded). The volumetric integral equation for the MoM formulation is given by:

$$\bar{E}_s(\bar{r}_m) + \bar{E}_i(\bar{r}_m) = E(\bar{r}_m) = \frac{\bar{J}_{eq}(\bar{r}_m)}{-j\omega\epsilon_0(\epsilon_r - 1)} \tag{1}$$

9

$$\bar{E}_s(\bar{r}_m) = \iiint\limits_V j\omega\mu_0 \overline{\overline{G}}(\bar{r}_m, \bar{r}') \cdot \bar{J}_{eq}(\bar{r}') dV' \qquad (2)$$

where subscripts s and i indicate the scattered and incident field, respectively, and the right side of (1) is an equivalent volumetric current. Also $\bar{r}_m$ is the center position of the mth cell, $\overline{\overline{G}}(\bar{r}_m, \bar{r}')$ is the free space electric dyadic Green's function which indicates the electric field at $\bar{r}_m$ generated by a point current source at $\bar{r}'$ and given by:

$$\overline{\overline{G}}(\bar{r}_m, \bar{r}') = \left(\overline{\overline{I}} + \frac{\nabla\nabla}{k_0^2} \right) \frac{e^{jk_0 R}}{4\pi R} \qquad (3)$$

where $\overline{\overline{I}}$ is the unit dyadic and R is the distance between $\bar{r}_m$ and $\bar{r}'$ which is $|\bar{r}_m - \bar{r}'|$. Substituting (2) into (1), one obtains

$$\bar{E}_i(\bar{r}_m) = \frac{\bar{J}_{eq}(\bar{r}_m)}{-j\omega\epsilon_0(\epsilon_r - 1)} - \iiint\limits_V j\omega\mu_0 \overline{\overline{G}}(\bar{r}_m, \bar{r}') \cdot \bar{J}_{eq}(\bar{r}') dV'. \qquad (4)$$

Discretizing this equation using a total of N cells for all the needles, a 3N × 3N matrix equation is obtained:

$$\begin{pmatrix} E_i^x \\ E_i^y \\ E_i^z \end{pmatrix} = \begin{pmatrix} Z_{xx} & Z_{xy} & Z_{xz} \\ Z_{yx} & Z_{yy} & Z_{yz} \\ Z_{zx} & Z_{zy} & Z_{zz} \end{pmatrix} \begin{pmatrix} J_{eq}^x \\ J_{eq}^y \\ J_{eq}^z \end{pmatrix} \qquad (5)$$

which can be solved for the unknown current coefficient J_{eq} in each cell, and where the 3 × 3 matrix in (5) is defined as the impedance or Z-matrix. Individual elements of the Z-matrix are given by

$$\overline{\overline{Z}}(\bar{r}_m) = \frac{\overline{\overline{I}}}{-j\omega\epsilon_0(\epsilon_r - 1)} - \iiint\limits_V j\omega\mu_0 \overline{\overline{G}}(\bar{r}_m, \bar{r}') dV' \qquad (6)$$

for the mth cell.

Equation (5) cannot be decomposed in the normal fashion into TM and TE incident fields in order to reduce the number of unknowns as each needle is oriented at a different angle so that a TM or TE incident wave only has meaning in the local coordinates of one single needle. Instead, we directly solve this problem in the coordinates of the whole cluster without decomposition.

In equation (5), the needle cluster stem is assumed to be oriented along the z-axis, in local coordinates. In the model of a pine tree, there are many needle clusters oriented at different angles. The Z-matrix is independent of the incident field (see (5)) and therefore need only be calculated once and reused for various incident angles, thus simplifying the MoM formulation.

2.3 Evaluation of the Z-Matrix

In order to evaluate the Z-matrix in an efficient fashion, the self-cell, the adjacent cells in the same needle, and the adjacent cells in different needles are treated in different ways as is discussed in the following sections.

10

2.3.1 Self-cell

Due to the singularity of the electric dyadic Green's function in the source region, the impedance matrix must be evaluated in an alternate fashion. A source dyadic $\overline{\overline{L}}$ is introduced according to [3]. As seen in Figure 3, the self-cell, with b the radius of its transverse cross-section and dl the length, is divided into two parts, an infinitesimally thin cylinder (radius of the transverse cross-section, a, approaching zero) along z-axis and the remainder of the volume.
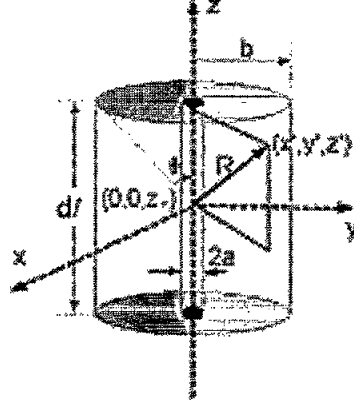
Figure 3: Self-cell configuration.

In the self-cell term contribution from the infinitesimally thin cylinder is given by $-\frac{\overline{\overline{L}}}{j\omega\epsilon_0}$ where [3]

$$\overline{\overline{L}} = \begin{pmatrix} 1/2 & 0 & 0 \\ 0 & 1/2 & 0 \\ 0 & 0 & 0 \end{pmatrix}. \tag{7}$$

The remainder is calculated by applying the principal value integral:

$$\lim_{a \to 0} \iiint_V j\omega\mu_0 \overline{\overline{G}}(\bar{r}_m, \bar{r}')dV', \tag{8}$$

where V stands for the volume of the self-cell excluding the infinitesimally thin cylinder.

According to (3), two integrals need to be evaluated:

$$I_1 = \lim_{a \to 0} \iiint_V \frac{e^{jk_0R}}{R}dV' \tag{9}$$

and

$$\overline{\overline{I}}_2 = \lim_{a \to 0} \iiint_V \nabla\nabla\frac{e^{jk_0R}}{R}dV', \tag{10}$$

11

where $R = \sqrt{x'^2 + y'^2 + (z' - z_m)^2} = \sqrt{\rho'^2 + (z' - z_m)^2}$. Since each cell is electrically small $(k_0 R << 1)$, (9) can be expanded in terms of a Taylor series as:

$$I_1 \simeq \lim_{a \to 0} \iiint_V \left(\frac{1}{R} + jk_0 \right) dV', \tag{11}$$

which after some algebra becomes:

$$I_1 \simeq jk_0 \Delta V + 2\pi \left[\frac{dl}{2} \sqrt{\left(\frac{dl}{2}\right)^2 + b^2} + b^2 \ln \left(\frac{dl/2 + \sqrt{b^2 + (dl/2)^2}}{b} \right) - \left(\frac{dl}{2}\right)^2 \right] \tag{12}$$

where $\Delta V = \pi b^2 dl$ is the volume of the cell.

To evaluate (10), one can first evaluate:

$$I_3 = \lim_{a \to 0} \iiint_V \frac{\partial^2}{\partial z^2} \frac{e^{jk_0 R}}{R} dV' = \lim_{a \to 0} -\frac{\partial}{\partial z} \iiint_V \frac{\partial}{\partial z'} \frac{e^{jk_0 R}}{R} dV', \tag{13}$$

where the identity $\frac{\partial}{\partial z} \frac{e^{jk_0 R}}{R} = -\frac{\partial}{\partial z'} \frac{e^{jk_0 R}}{R}$ is applied.

By integrating over z' on of the partial derivatives, $\frac{\partial}{\partial z'}$ in (13) is eliminated. Evaluation of the remaining integral and then evaluation of the second partial derivative in (13) gives:

$$I_3 = 4\pi \left[e^{jk_0 \sqrt{b^2 + (dl/2)^2}} \frac{dl/2}{\sqrt{b^2 + (dl/2)^2}} - e^{jk_0 dl/2} \right]. \tag{14}$$

The other two diagonal elements are difficult to evaluate directly. However, they can be evaluated alternatively according to the Helmholtz equation:

$$\iiint_V \left(\frac{\partial^2}{\partial x^2} + \frac{\partial^2}{\partial y^2} + \frac{\partial^2}{\partial z^2} + k_0^2 \right) \frac{e^{jk_0 R}}{R} dV' = 0, \tag{15}$$

since the integration is performed over a source-free region (the source point is inside the infinitesimally thin cylinder and has been excluded). In addition, it can be noticed that there is no difference between the integration with respect to x and y. Therefore, one obtains:

$$I_4 = \iiint_V \frac{\partial^2}{\partial x^2} \frac{e^{jk_0 R}}{R} dV' = \iiint_V \frac{\partial^2}{\partial y^2} \frac{e^{jk_0 R}}{R} dV' = -\frac{1}{2}(I_3 + k_0^2 I_1) \tag{16}$$

The off-diagonal elements of $\overline{\overline{I_2}}$ are equal to zero since the cell is symmetric about z-axis.

An alternative way to evaluate the self-cell is to treat the whole cell as the source region which contributes as a source dyadic [3]:

$$\overline{\overline{L}} = \begin{pmatrix} \frac{1}{2} \cos \theta & 0 & 0 \\ 0 & \frac{1}{2} \cos \theta & 0 \\ 0 & 0 & 1 - \cos \theta \end{pmatrix}. \tag{17}$$

Provided that the dimensions of the self-cell are small enough, this approach can give similar results as that given by the previous method.
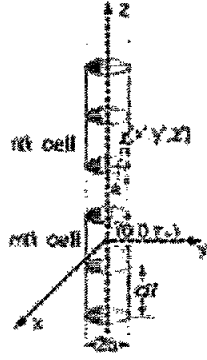
Figure 4: Configuration of two adjacent cells in the same needle.

2.3.2 Adjacent cells in the same needle

Figure 4 shows the individual cells in a single needle. The electric field at the center of the mth cell generated by the nth cell is calculated by evaluating similar integrals as for the self-sell. The difference lies in that for this case the observation point (center of the mth cell) is out of the integration region (the nth cell), therefore no singularity needs be concerned. Also for the integral $I_5 = \iiint \frac{e^{jk_0R}}{R} dV'$, such kind of approximation as (11) is not suitable due to the relatively large distance between the two cells. Instead, I_5 is evaluated as the following:

$$
\begin{aligned}
I_5 &= \int_{-dl/2}^{dl/2} \int_0^{2\pi} \int_0^b \frac{e^{jk_0R}}{R} \rho' d\rho' d\phi' dz' \\
&= \frac{2\pi}{jk_0} \int_{-dl/2}^{dl/2} \left(e^{jk_0\sqrt{b^2+(z_m-z_n-z')^2}} - e^{jk_0\sqrt{(z_m-z_n-z')^2}} \right) dz',
\end{aligned}
$$

(18)

where z_m, z_n are the z-coordinates of the mth and nth cell, respectively. The evaluation of integral $\int_{-dl/2}^{dl/2} e^{jk_0\sqrt{b^2+(z_m-z_n-z')^2}} dz'$ can be approximated by expanding the integrand into Taylor series up to the cubic term.

The evaluation of the elements of $\overline{\overline{I_6}} = \iiint_{n\text{th cell}} \nabla\nabla \frac{e^{jk_0R}}{R} dV'$ are performed the same way as evaluating $\overline{\overline{I_2}}$. First, we compute:

$$
\begin{aligned}
I_7 &= \iiint_{n\text{th cell}} \frac{\partial^2}{\partial z^2} \frac{e^{jk_0R}}{R} dV' = -\frac{\partial}{\partial z} \int_0^{2\pi} \int_0^b \int_{-dl/2}^{dl/2} \frac{\partial}{\partial z'} \frac{e^{jk_0R}}{R} dz' \rho' d\rho' d\phi' \\
&= -2\pi \left[e^{jk_0\sqrt{b^2+(z_m-z_1)^2}} \frac{z_m - z_1}{\sqrt{b^2 + (z_m - z_1)^2}} - e^{jk_0(z_m-z_1)} \right. \\
&\qquad \left. - e^{jk_0\sqrt{b^2+(z_m-z_2)^2}} \frac{z_m - z_2}{\sqrt{b^2 + (z_m - z_2)^2}} + e^{jk_0(z_m-z_2)} \right].
\end{aligned}
$$

(19)

where $z_1 = z_n + dl/2, z_2 = z_n - dl/2$. The other two diagonal elements are computed the

13

similar way as for the self-cell (see (15) and (16)). Again, the off-diagonal elements equal zero due to the symmetry of the cylinder.

The integrals above, including that for the self-cell, are evaluated in the local coordinates of a single needle. When modeling the whole needle cluster, global coordinates of the cluster must be used. A coordinate transformation matrix [2] is employed to transform the impedance matrix from each needle's local coordinates to the global coordinates.

2.3.3 Cells in different needles

Evaluating individual cells in different needles (Figure 5) is more difficult as they are not oriented identically. Performing a coordinate transformation for each needle will greatly increase the problem complexity. In addition, those volume integrals in (18) and (19) are difficult to evaluate in this case since the two cells are not coaxial.
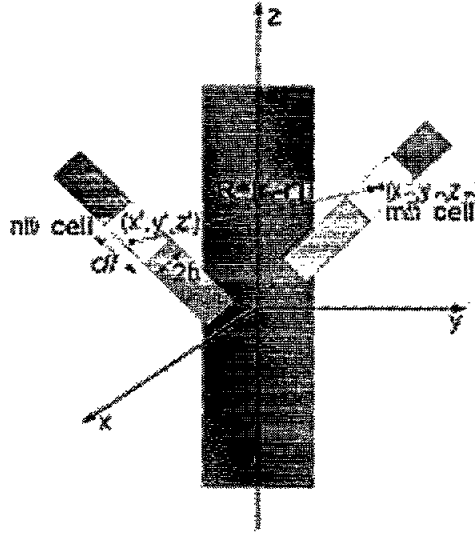
Figure 5: Configuration of two adjacent cells in different needles.

However, due to the relatively far distance between these two cells, it is possible to make the following mid-point approximation [4]:

$$\iiint_{nth\ cell} j\omega\mu_0\overline{\overline{G}}(\bar{r}_m, \bar{r}')dV' \simeq \Delta V j\omega\mu_0\overline{\overline{G}}(\bar{r}_m, \bar{r}_n).$$ (20)

and the elements of $\overline{\overline{G}}(\bar{r}_m, \bar{r}_n)$ are given by

$$G^{mn}_{x_p x_q} = \frac{j\omega\mu_0 k_0 \Delta V exp(j\alpha_{mn})}{4\pi\alpha^3_{mn}}[(\alpha^2_{mn} - 1 + j\alpha_{mn})\delta_{pq} + \frac{(x^m_p - x^n_p)(x^m_q - x^n_q)}{R^2_{mn}}(3 - \alpha^2_{mn} - 3j\alpha_{mn})],$$ (21)

where p and q both take on the values 1,2, and 3, independently, so that they represent the coordinates x, y, and z. Also, $R_{mn} = |\bar{r}_m - \bar{r}_n|$, and $\alpha_{mn} = k_0 R_{mn}$. The Kronecker delta $\delta_{pq} = 0$ if $p \neq q$ and $\delta_{pq} = 1$ if $p = q$.

In (20), every cell is in the global cluster coordinates and a coordinate transformation is not necessary.

Table 1: Region of Validity of Rayleigh-Gans Approximation for Several Frequency Points (b =0.6 mm, $\theta_i = 60°$). Note that the 10 GHZ and 20 GHz cases are outside the Rayleigh-Gans region of Validity.

Frequency (GHz)	λ_0 (mm)	ϵ_r	$2k_0b \left\| \sqrt{\epsilon_r - \cos^2(\theta_i)} \right\|$
3	100	21.79 + j 6.20	0.357
6	50	19.85 + j 6.45	0.685
10	30	17.73 + j 7.26	1.094
20	15	13.39 + j 7.71	1.9620

2.4 Z-matrix and Some Results

To solve the matrix equation the Z-matrix need only be inverted once to calculate the unknown currents for different excitations as:

$$\bar{J}_{eq} = \overline{\overline{Z}}^{-1} \bar{E}_i \tag{22}$$

Note that according to reciprocity theorem, the Z-matrix is symmetric. Therefore, the number of elements requiring storage is reduced from $3N \times 3N$ to $3N \times (3N + 1)/2$.

For tree modeling, $\overline{\overline{Z}}^{-1}$ can be reused for different needle clusters. To obtain $\overline{\overline{Z}}^{-1}$, (5) should be solved directly, which requires significant RAM. To make the problem tractable, a needle cluster containing 10 needles is considered.

The needle cluster model is similar to that in Figure 2. Needles stem from the cluster spirally and the tilt angle decreases when approaching the tip of the stem. Needles have the same length l (50 mm) and transverse cross-section radius b (0.6 mm). The incident angles are selected to be $\theta_i = 60°, \phi_i = 45°$. Forward scattering is evaluated for both multiple scattering and single scattering cases. For the latter case, it is equivalent to setting the impedance matrix elements between cells in different needles to zero.

2.4.1 Single Scattering

First, the single scattering case is examined. For this case, it is equivalent to setting the interaction between cells in different needles to zero. For validation, the result is then compared to those which use the Rayleigh-Gans approximation to calculate single scattering [2].

Both algorithms assume the transverse dimension of the needle is small enough. To be specific, in the Rayleigh-Gans region $2k_0b \left| \sqrt{\epsilon_r - \cos^2(\theta_i)} \right| < 1$ should be satisfied [5], where ϵ_r is the relative dielectric constant of the needle.

Several frequency points are evaluated. The dielectric characteristics of the pine needle under these frequencies are listed in Table 1.

As seen from Table 1, for b =0.6mm, the valid region of our MOM algorithm is below 10 GHz. Figure 6 shows the scattered field components in the forward scattering direction with variable azimuth scattering angles at 3 GHz.

Both algorithms (Rayleigh-Gans and MOM) agree very well. The largest deviation is less than 0.5 dB.

Figure 7 and 8 plots the forward scattering (under H-polarization and V-polarization incidence, respectively) at 20 GHz, which is far out of the Rayleigh-Gans region.
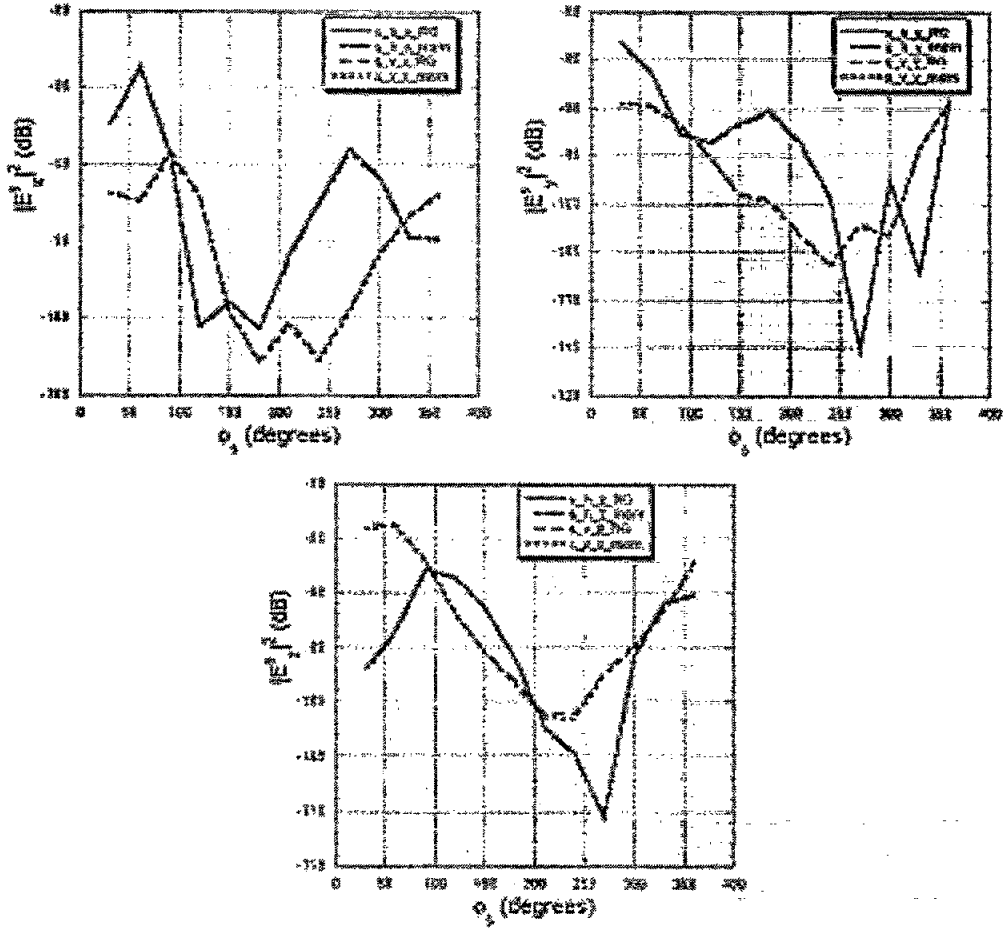
15

Figure 6: Component of the forward scattered field versus the azimuth angle (both H- and V- polarization incidence, frequency = 3 GHz).
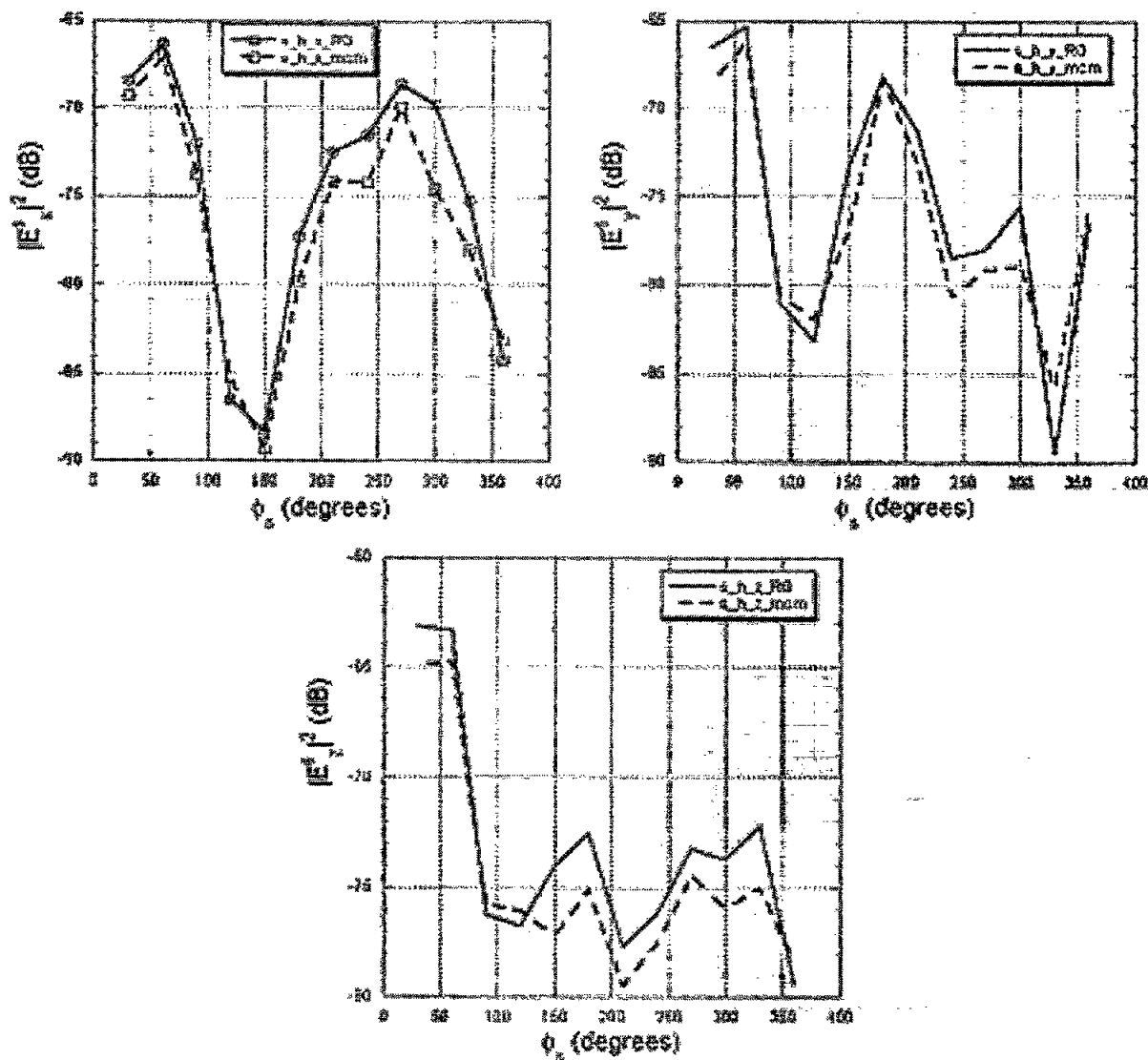
Figure 7: Components of the forward scattered field versus the azimuth angle (H-polarization incidence, frequency = 20 GHz).
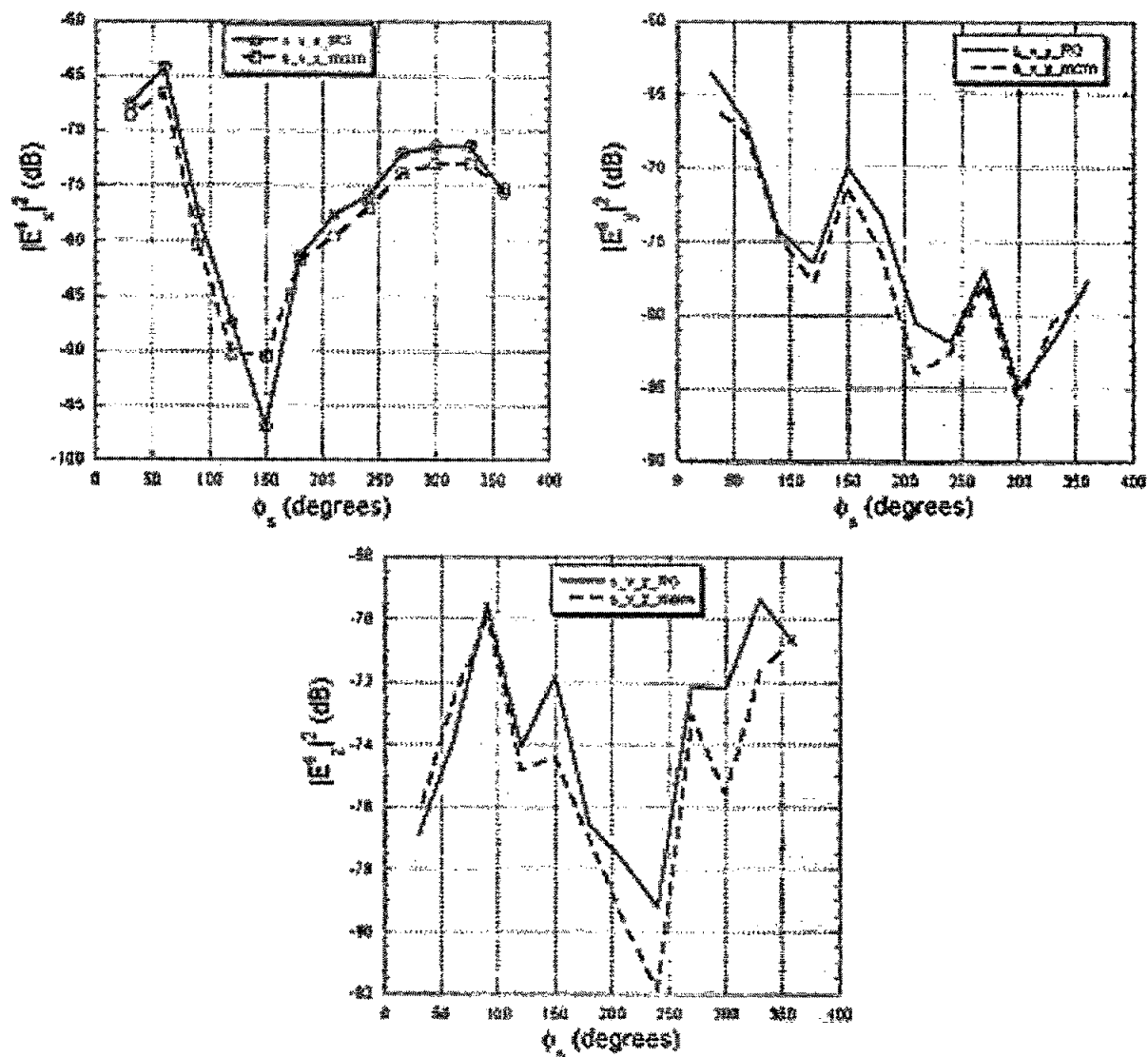
Figure 8: Components of the forward scattered field versus azimuth angle (V-polarization incidence, frequency = 20 GHz).

Both algorithms are not accurate in this case since the basic assumption of constant current in each individual cell is no longer valid any more. To achieve more accuracy, two kinds of improvements on the MOM algorithm should be applied. The first is to use a more complex basis function. In addition, Galerkin's method can be employed instead of Point-matching as a weighting function to improve accuracy. Also, one could divide the cluster into finer cells. These improvements however, will increase both the complexity of the problem and the computing resources needed dramatically.

2.4.2 Multiple Scattering

In this section the effects of multiple scattering between needles is included in the MoM calculations. Two cases are examined. One at 3 GHz with $b = 0.6$ mm. The other is at 35 GHz with $b = 0.1$ mm. Both are in the Rayleigh-Gans region of validity.

Figure 9 compares the difference between single scattering (based on Rayleigh-Gans approximation) and multiple scattering using MoM at 3 GHz. It is seen that the multiple scattering effect on the scattered field is around 1 dB at most for this case.

Figure 10 shows the difference between single scattering (based on Rayleigh-Gans approximation) and multiple scattering at 35 GHz. The relative dielectric constant of the pine needle at this frequency cannot be calculated by using standard mixing formulas. It is assumed to be $9 + j4$ in the simulation. With this value, $b = 0.1$ mm is selected to assure the validity of both Rayleigh-Gans approximation and MOM algorithms. It is seen that the multiple scattering effect on the scattered field is minimal for this case. This could be due to the very thin transverse cross-section radius of the needle. In practice, the radius is much larger than 0.1 mm, and the MOM algorithm needs further improvement to accurately evaluate this case, as discussed.

2.5 Conclusions

A MOM formulation is used to evaluate the multiple scattering effects of pine needles in a cluster. For very thin needles, where the Rayleigh-Gans approximation is valid, this algorithm provides accurate results. For instance, at 3 GHz, with the radius of the transverse cross-section of the needles at 0.6 mm, the difference between single and multiple scattering is around 1 dB. At 35 GHz, a needle with a 0.6 mm radius is out of the region of validity of the Rayleigh-Gans approximation and is computational intractable for the MoM formulation. Both finer division of needles and higher order basis functions could achieve this goal, at the expense of increasing the complexity of the formulation the computing resources required.

Figure 9: Comparison of single and multiple scattering for each component of the forward scattered field versus the azimuth angle (H- and V- polarization incidence, frequency = 3 GHz, "sin" and "mul" stand for single scattering and multiple scattering).
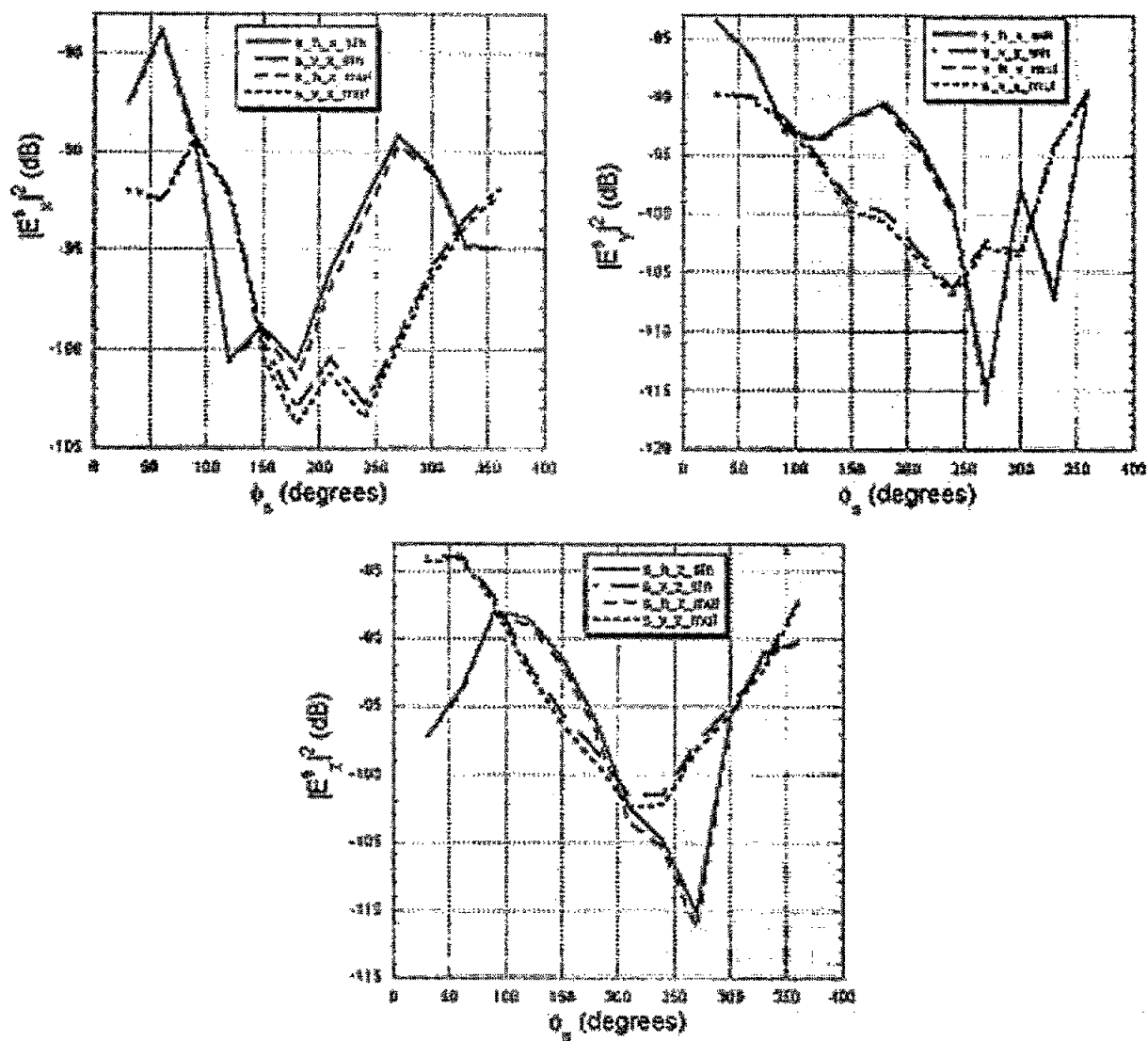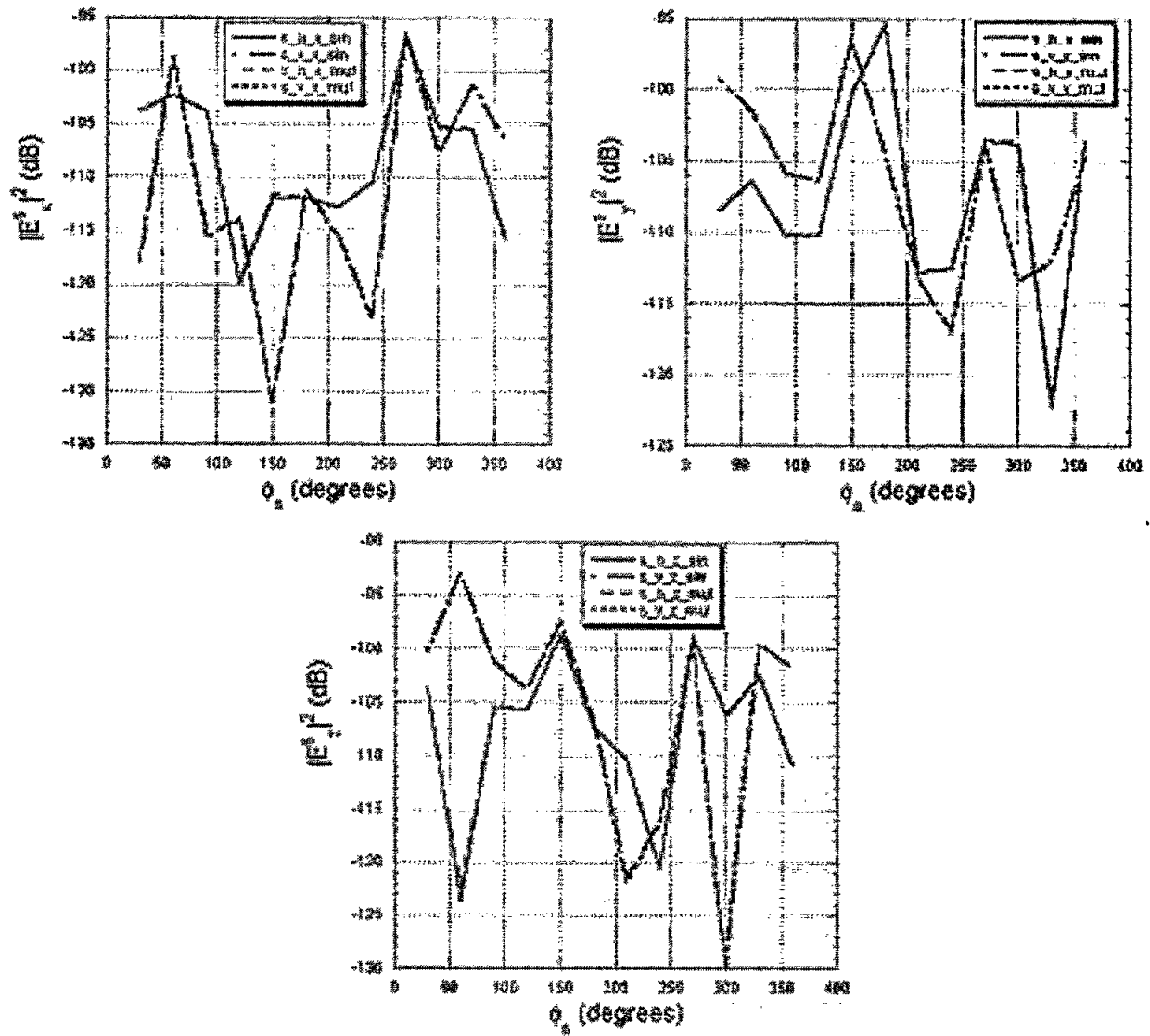
Figure 10: Comparison of single and multiple scattering for each component of the forward scattered field versus the azimuth angle (H- and V- polarization incidence, frequency = 35GHz, "sin" and "mul" stand for single scattering and multiple scattering).

3 Fast Multipole Representation of Green's Function for Impedance Surface and Its Application in Simulation of Cosite Interference for CDMA Systems

3.1 Introduction

The Sommerfeld problem, radiation of a short dipole above an infinite dielectric half-space, is a classic problem in electromagnetics that has received significant attention throughout the years. However, because of its importance in a wide range of applications, it still has remained contemporary. The formal solution is represented by integrals whose integrands are highly oscillatory and slowly decaying. These properties make the direct numerical integration computationally very inefficient. For impedance surfaces however, an efficient method known as exact image theory has been implemented [6]. Since this formula replaces the poorly converging integrands of the Sommerfeld integral with exponentially decaying integrands, calculation of the fields from an arbitrary source above an impedance surface can be performed very efficiently, independent of the relative locations of the source and observation points. Hence using this exact image representation, it is much easier to compute scattering from a complex object above an impedance half-space using a common numerical method such as the method of moments (MoM). However numerical complexity of MoM is at best $O(n^2)$, which prohibits the MoM to be applied to electrically large objects. To overcome this difficulty, in recent years several methods have been proposed. These include fast multipole method (FMM) [7], adaptive integral method (AIM) [8], and many other variations of FMM and AIM. FMM has been rigorously formulated for the free-space Green's function, and successfully applied to a large class of problems ranging from passive circuit analysis to computation of the radar cross section (RCS) of complex objects. In recent years the FMM algorithm has been extended to include scattering problems in the presence of a dielectric half space using the method of complex images [9]. The method of complex images approximates a component of the integrand of the Sommerfeld integral by Prony's method in terms of a summation of exponential functions which can then be integrated analytically. The result is a summation of discrete image points in the complex Z-plane. The drawback of this method is that depending upon the location of observation and source points (especially if they are close to the surface) the number of exponential terms in the Prony's approximation has to be increased. In this work using the exact image formulation, an efficient multipole representation of the Green's function for impedance surfaces is obtained and is shown to be very accurate for all locations of source and observation points. In Section 3.2 the multipole representation is formulated, then in Section 3.3 the convergence property of the formulation is investigated, and the accuracy of the results is verified by comparing them with those obtained from direct numerical integration of the exact images.

3.2 Fast Multipole Representation of Green's Function for Impedance Surfaces

The geometry of an elementary current source above an impedance surface is shown in Figure 11. As shown the infinitesimal dipole is oriented along $\hat{l}$ and located at (x', y', z') above a surface with a normalized impedance of $\eta = Z_0/Z_1$. The observation point chosen at (x, y, z) is also shown in this figure. A closed form expansion for the total field in the presence of the

impedance surface using the exact image theory is found to be [6]:

$$\vec{\mathbf{E}} = \vec{\mathbf{E}}^d + \vec{\mathbf{E}}^i + i2k_0Z_0 \left[\frac{e^{ik_0R}}{4\pi R} - \alpha \int_0^\infty e^{-\alpha\xi} \frac{e^{ik_0R'}}{4\pi R'} d\xi \right] (l_x\hat{x} + l_y\hat{y}) -$$

$$i2Z_0\eta l_z\hat{z} \left[\left(i\frac{\partial}{\partial z} + \beta \right) \frac{e^{ik_0R}}{4\pi R} + (k_0^2 - \beta^2) \int_0^\infty e^{-\beta\xi} \frac{e^{ik_0R'}}{4\pi R'} d\xi \right] +$$

$$2Z_0\eta\hat{l} \times \left(\frac{\partial}{\partial y}\hat{x} - \frac{\partial}{\partial x}\hat{y} \right) \left[\frac{e^{ik_0R}}{4\pi R} - \beta \int_0^\infty e^{-\beta\xi} \frac{e^{ik_0R'}}{4\pi R'} d\xi \right] +$$

$$i\frac{2Z_0\eta}{1-\eta^2} \left\{ \frac{\partial^2}{\partial x^2} l_x\hat{x} + \frac{\partial^2}{\partial y^2} l_y\hat{y} + \frac{\partial^2}{\partial x \partial y}(l_y\hat{x} + l_x\hat{y}) \right\} \int_0^\infty (e^{-\alpha\xi} - \eta^2 e^{-\beta\xi}) \frac{e^{ik_0R'}}{4\pi R'} d\xi \quad (23)$$

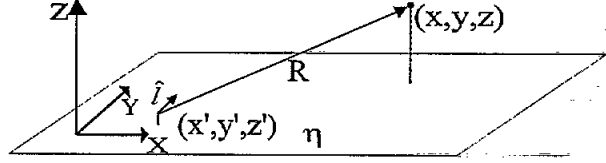Here $\vec{\mathbf{E}}^d$ and $\vec{\mathbf{E}}^i$ are fields from

Figure 11: An arbitrarily oriented infinitesimal dipole locates at (x', y', z') over an impedance surface with a normalized impedance, $\eta = Z_0/Z_1$.

the dipole itself and its image in a perfect conductor, respectively. Also in (23) $\alpha = k_0/\eta$, $\beta = k_0\eta$, $R' = \sqrt{(x - x')^2 + (y - y')^2 + (z + z' + i\xi)^2}$, $R = \sqrt{(x - x')^2 + (y - y')^2 + (z + z')^2}$. Before proceeding with the development of the FMM representation of the total field (Green's function), it is worth noting the convergence properties of the integrals in (23). The two exponential decaying factors (α, β) are obvious in all integrals, but besides these, R' itself is a complex quantity with a positive imaginary part which is responsible for an additional exponential decay of the integrands. These exponential decaying terms ensure fast and accurate computation of the Green's function for half-space impedance problems. Physically $e^{-\alpha\xi}$ or $e^{-\beta\xi}$ can be interpreted as continuous current distribution in the complex Z plane $(Z = z + i\xi)$ representing the image of a source point in an impedance surface. For capacitive surfaces, such as the earth, $|\eta| < 1$ and therefore the decay factor for the horizontal polarization is much higher than the vertical polarization. In extreme cases where $|\eta| \ll 1$ the decay factor of the integrand for the vertical polarization is dominated by R' as mentioned earlier.

Multipole representation of dyadic Green's function for applications in integral equations method has been proven to be useful with regard to computational speed and resources. Examining equation (23) it is obvious that the well-known FMM algorithms can be used for $\vec{\mathbf{E}}^d$ and $\vec{\mathbf{E}}^i$ directly [7]. However for the rest of expressions in (23), a new multipole representation is needed in order to decompose the Green's function in terms of sum of the products of two functions, one dependent on the source coordinate and the other one dependent on the observation coordinate. To achieve this goal, a multipole expansion for $I = \int_0^\infty e^{-p\xi} \frac{e^{ik_0R'}}{R'} d\xi$ is needed where p represents α or β. One can attempt to express $\frac{e^{ik_0R'}}{R'}$ in the integrand of I in terms of its multipole expansion. However since the domain of ξ extends to infinity such substitution cannot be rigorously justified despite the fact that due

to the exponential decay the integral does not contribute significantly for large value of ξ. We will revisit this approach after deriving a formal solution.

To derive a formal multiple expansion for the Green's function, a new integral expression for I is obtained. Integrating I by parts and noting $\frac{\partial}{\partial \xi}\frac{e^{ik_0 R'}}{R'} = i\frac{\partial}{\partial z'}\frac{e^{ik_0 R'}}{R'}$, it can be shown that I must satisfy the following first-order differential equation.

$$\frac{\partial I}{\partial z'} + ipI = i\frac{e^{ik_0 R}}{R} \tag{24}$$

The general solution of (24) for I is composed of the particular solution and the homogeneous solution given by

$$I = ie^{-ipz'}\int \frac{e^{ik_0 R}}{R}e^{ipz'}dz' + Ce^{-ipz'} \tag{25}$$

where C is a constant function of z'. Note that new integral representation is highly oscillatory and not amenable for numerical evaluation. However, as will be shown next this expression is suitable for multipole expansions. But first the coefficient C in (25) must be determined. To find C it is noted that $\lim_{z'\to\infty} e^{-ipz'} = \infty$ in the upper half-plane of p plane where $\Im[p] > 0$. However, since I must approach zero due to the radiation condition, C must be zero when $\Im[p] > 0$. Noting that I is an analytic function of p, then according to "analytic continuation", C must be zero for all values of p (the entire plane). Now a multipole representation of I can be obtained using the Gegenbauer's addition theorem. According to Figure 12

$$\frac{e^{ik_0 R}}{R} = \frac{e^{ik_0|\vec{r}-\vec{r'}|}}{|\vec{r}-\vec{r'}|} = \frac{e^{ik_0|\vec{X}+\vec{d}|}}{|\vec{X}+\vec{d}|}$$

Figure 12: Definition of vectors, $\vec{X}$, and $\vec{d}$ in the formulation of multipole representation of equation (26).

Requiring $|\vec{d}| < |\vec{X}|$, Gegenbauer's addition theorem [10] states that

$$\frac{e^{ik_0 R}}{R} = ik_0\sum_{n=0}^{\infty}(-1)^n(2n+1)P_n(\cos\theta)h_n(k_0 X)j_n(k_0 d) \tag{26}$$

where $d = |\vec{d}| = \sqrt{(x'-x_c)^2 + (y'-y_c)^2 + (z'-z_c)^2}$,
$X = |\vec{X}| = \sqrt{(x_c-x)^2 + (y_c-y)^2 + (z_c+z)^2}$, and θ is the angle between $\vec{X}$ and $\vec{d}$ vectors given by $\theta = \cos^{-1}(\vec{X}\cdot\vec{d})$ as shown in Figure 12. Also here P_n is the Legendre polynomial, and

h_n and j_n are the spherical Bessel functions. Using the plane wave expansion representation of $P_n j_n$ [7]

$$P_n(\cos\theta)j_n(k_0 d) = \frac{(-i)^n}{4\pi}\int_{4\pi} d^2\hat{k}\, e^{i\vec{k}\cdot\vec{d}} P_n(\hat{k}\cdot\hat{X}) \qquad (27)$$

where $\vec{k} = k_0(\sin\nu\cos\psi\hat{x} + \sin\nu\sin\psi\hat{y} + \cos\nu\hat{z})$ and $\hat{k} = \vec{k}/k_0$. Substituting (27) in (26) and then performing integration with respect to z', I can be written as

$$I = \frac{ik_0}{4\pi}\sum_{n=0}^{\infty} i^n(2n+1)h_n(k_0 X)\int_{4\pi} d^2\hat{k}\, P_n(\hat{k}\cdot\hat{X})\frac{e^{i\vec{k}\cdot\vec{d}}}{k_0\cos\nu + p} \qquad (28)$$

This formal solution, when the series converges, is believed to be an exact representation of the multipole expansion for the Green's function. This will also be verified numerically and the regions where the series converges will be identified. It is important to note that equation (28) except for the factor $\frac{1}{k_0\cos\nu + p}$ is identical to that of the free space multipole representation of the Green's function, and therefore is of the same computational complexity. As will be shown later identity (28) converges very quickly when $|p/k| > 1$, which is the case for horizontal polarization ($p = \alpha = k_0/\eta$) and when the magnitude of the surface normalized impedance is less than unity $|\eta| < 1$. These values of surface normalized impedance corresponds to impedance of ground at UHF band and below or water surfaces below 10 GHz.

Unfortunately, the series convergence may become rather poor for vertical polarization when $p = \beta$. As $\Re[p]$ decreases, each term in the summation decays slowly with n, and the partial summation starts to oscillate. This increases the required number of terms in the summation for convergence and hence the expansion becomes numerically unstable. The formal derivation of (28) seems to be exact and therefore lack of convergence of the series under certain conditions for the vertical polarization must be further examined. This problem can be a result of interchanging the order of the infinite summation and the integration. This interchange is not always allowed according to the Lebesque's dominated convergence theorem.

To verify the validity of (28) (where the series converges) another independent approach may be followed. Noting the exponential decays in the integrand of I, the integral range can be truncated i.e.,

$$I = \int_0^\infty e^{-p\xi}\frac{e^{ik_0 R'}}{R'}d\xi \approx \int_0^a e^{-p\xi}\frac{e^{ik_0 R'}}{R'}d\xi \qquad (29)$$

where a is chosen so that

$$e^{\Re[ik_0 R' - p\xi]}\big|_{\xi=a} = e^{-\frac{k_0}{\sqrt{2}}\sqrt{\sqrt{(R^2-a^2)^2 + 4R^2 a^2\cos^2\theta} - R^2 + a^2} - \Re[p]a} \ll 1$$

This choice of a also satisfies the condition for which the following addition theorem for the scalar Green's function is valid. Using the Gegenbauer's addition theorem for complex quantities, the integrand (scalar Green's function with complex range function) is expanded as

$$\frac{e^{ik_0 R'}}{R'} = ik_0\sum_{n=0}^{\infty}(-1)^n(2n+1)P_n(\cos\theta_2)h_n(k_0 X)j_n(k_0 d) \qquad (30)$$

25
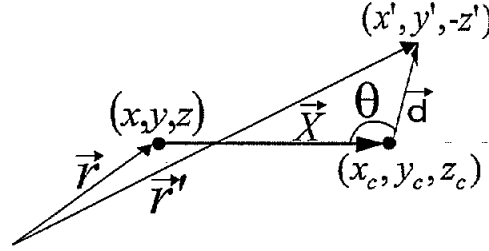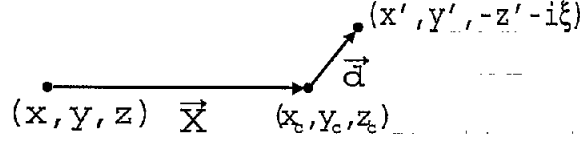
Figure 13: Definition of vectors, $\vec{X}$, and $\vec{d}$ in the formulation of multipole representation of equation (30).

Also $X = \sqrt{(x_c - x)^2 + (y_c - y)^2 + (z_c + z)^2}$, $d = \sqrt{(x' - x_c)^2 + (y' - y_c)^2 + (z' + z_c + i\xi)^2}$, and θ_2 is a complex angle between $\vec{X}$ and $\vec{d}$ vectors given by $\theta_2 = \cos^{-1}(\vec{X} \cdot \vec{d})$ (see Fig. 13). This expansion is valid for the condition $|X| > |de^{\pm i\theta}|$. Using the identity given by (27),

$$I \approx \frac{ik_0}{4\pi} \sum_{n=0}^{\infty} i^n(2n+1)h_n(k_0 X) \int_{4\pi} d^2\hat{k} P_n(\hat{k} \cdot \hat{X}) e^{i\vec{k}\cdot\vec{d}} \frac{1 - e^{-(k_0 \cos \nu + p)a}}{k_0 \cos \nu + p} \tag{31}$$

In limit as a goes to infinity, the exponential function in the integrand of (31) disappears and the expression reduces to the formal solution previously derived. Therefore The formal solution converges for a large value of $\Re[p]$, but the convergence rate becomes poorer when $\Re[p]$ decreases.

For $p = \beta$ and in situations when convergence is poor (the region of poor convergence which will be specified later) an approximate identity can be formulated. However this approximate formulation is much less efficient than the expansion given by (28). Using a Gaussian quadrature numerical integration applied to the exact image representation, I can be approximated as a finite summation of the form that resembles the method of complex images, i.e.,

$$I \approx \sum_{n=1}^{N} w_n e^{-p\xi_n} \frac{e^{ik_0 R'_n}}{R'_n} \tag{32}$$

where $R'_n = \sqrt{(x - x')^2 + (y - y')^2 + (z + z' + i\xi_n)^2}$ with w_n and ξ_n being the weighting factor and zero of the Legendre Polynomial of nth order. The discrete terms $\frac{e^{ik_0 R'_n}}{R'_n}$ in (32) can be expanded using (26). Because of exponential decay in the integrand $(e^{-p\xi})$, the order N can be chosen so that the accuracy of (32) be independent of source and observation coordinates.

3.3 Simulation Results

For a source at a frequency of 50MHz, and for a surface with a normalized surface impedance $\eta = 0.3 - i0.1$ ($p = \alpha = 3.14 + 1.05i$ and $p = \beta = 0.31 - 0.11i$) the FMM expressions for I are compared with the direct numerical calculations. For simplicity (x, y, z) is located at $(0,0,0)$ and (x_c, y_c, z_c) is at $(7,0,2.2)$. For numerical simulations, the following identity is used, which can be derived directly from (28):

$$\frac{e^{ik_0 R}}{4\pi R} - p\int_0^{\infty} e^{-p\xi} \frac{e^{ik_0 R'}}{4\pi R'} d\xi = \frac{ik_0}{(4\pi)^2} \sum_{n=0}^{\infty} i^n(2n+1)h_n(k_0 X) \int_0^{2\pi} \int_0^{\pi} P_n(\hat{k}\cdot\hat{X}) \frac{k_0 e^{i\vec{k}\cdot\vec{d}} \cos \nu}{k_0 \cos \nu + p} \sin \nu d\nu d\psi \tag{33}$$

26

Figure 14 shows the magnitude of each term of the summation given by (33) for $p = \alpha$ as a function of n for two different surface impedances, $\eta = 0.3 - i0.1$ ($\Re[p] = 3.14$), and $\eta = 0.8 - i0.1$ ($\Re[p] = 1.3$). In this figure it is clearly shown that as the real part of p decreases, the convergence of the summation becomes poorer (terms decay much slower), and the partial sum begins to oscillate as mentioned earlier. The following figures show comparisons of the results obtained from the FMM expression given by (28) and (32) with those obtained from direct numerical integration. Figure 15 is a plot of the difference between the direct numerical integration (left-hand side of (33)) and its FMM representation (right-hand side of (33)) as a function of real, and imaginary part of p/k. For this calculation observation and source points are, respectively, fixed at (7.5,0,2.2) and (0,0,0), and the number of summation terms (N) is 10. As seen in this figure except for the case of $\Im[p/k] < 0.5$ and $\Re[p/k] < 1.2$ the expansion given by (28) gives excellent results. Hence for all practical purposes the identity given by (28) can be used except when $\Re[p/k] < 1.2$ and $\Im[p/k] < 0.5$. In this region ($\Re[p/k] < 1.2$ and $\Im[p/k] < 0.5$) the less efficient formula given by (32) may be used. By changing the location of source and observation points, it was determined that the region of validity of (28) is independent of the coordinates of the source and observation points. For a numerical comparison, an example is considered when the observation point is moved along a parameterized curve $x = x_c + 0.5\cos\phi$, $y = y_c + 0.5\sin\phi$, and $z = z_c$. Figures 16(a) and 16(b) show comparisons of the magnitude, and the phase of the left- and right-hand side of (33) for $p = \alpha = 3.14 + 1.05i$, respectively. These two results are in an excellent agreement. The next figure shows the same comparisons for $p = \beta = 0.31 - 0.11i$. For this case (choosing $N = 10$), discrepancies of less than 0.2 dB in the magnitude and 1° in phase are observed.

3.4 Conclusions

Two multipole representations of the field of a dipole above impedance surfaces are formulated. These formulations are suitable for FMM type algorithms applied to scattering problems from an object over/on an impedance surface. One formulation is exact and valid for the range of $\Re[p/k] > 1.2$ and $\Im[p/k] < 0.5$, and the other, which is approximate and computationally less efficient, for the complement region. These representations are verified by comparing them with a direct numerical integration. It was also shown that the exact multipole expansion for the scalar Green's function of the half-space problem is very similar to that of the free-space and so is of the same computational complexity.
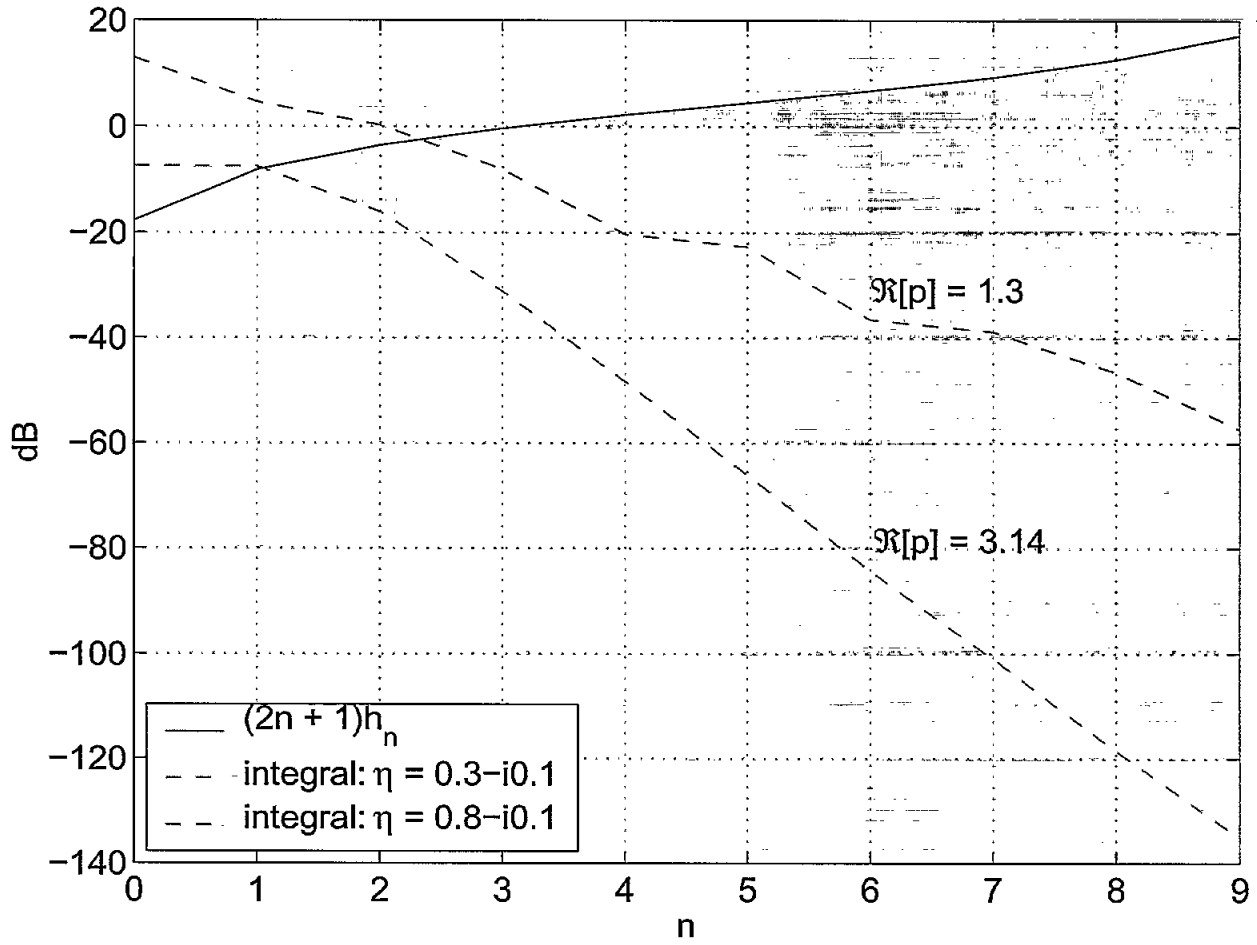
Figure 14: Convergence behavior of (28) as a function of $\Re[p]$. Magnitude of each term of the summation is shown.
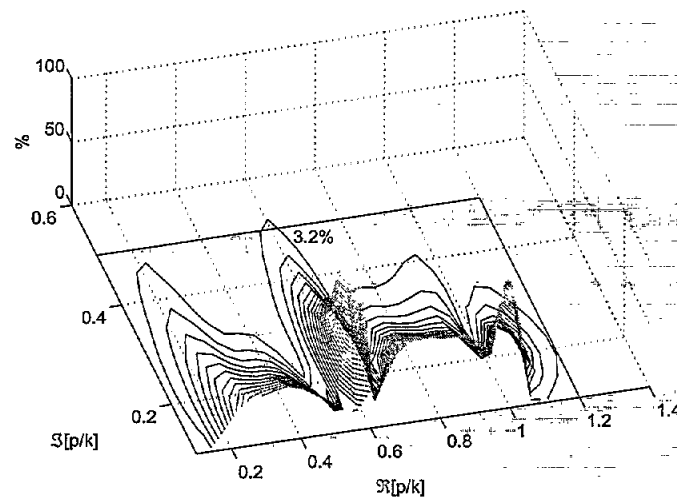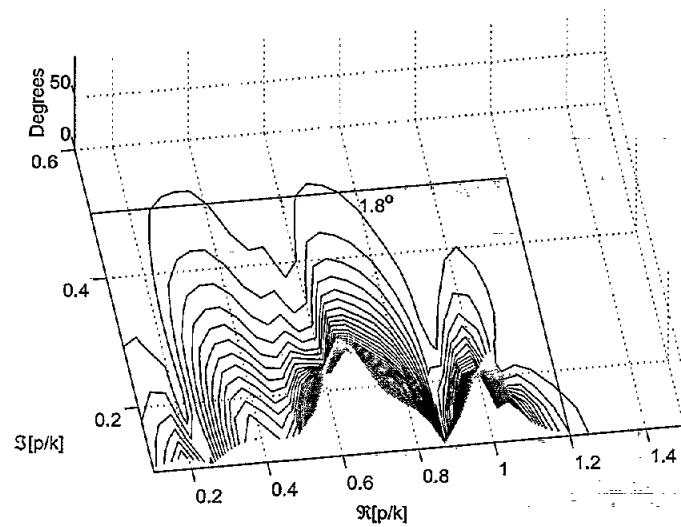
Figure 15: Error between LHS of (33) (numerical integration) and RHS of (33) (FMM identity) as a function of p/k at 50MHz. Observation point is fixed at (7.5,0,2.2). (a) Percentage error of magnitude (< 100 %), (b) Phase difference ($< 90°$).
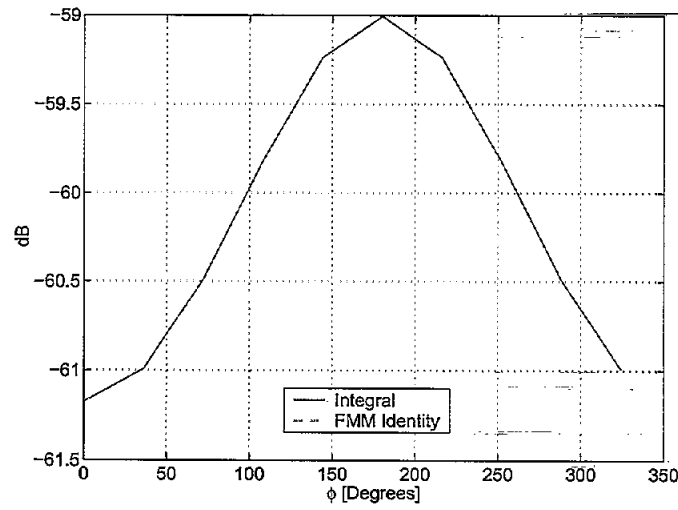
(a)
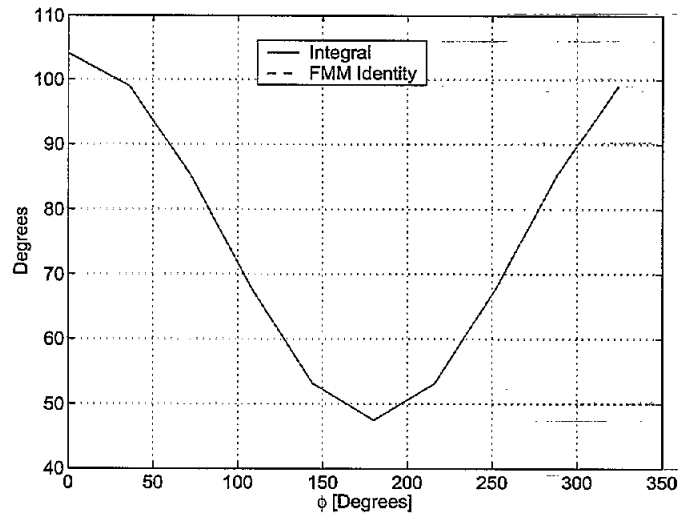
(b)

Figure 16: Comparison of LHS of (33) (numerical integration) and RHS of (33) (FMM identity) when $p = \alpha = 3.14 + 1.05i$ as a function of observation point position, $(7 + 0.5\cos\phi, 0.5\sin\phi, 2.2)$. (a) Magnitude (b) Phase.

4 Rural and Urban Propagation Simulator

Integration of an accurate rendition of the physical environment with an appropriate electromagnetic simulator is crucial in high fidelity propagation modeling. Software developed to date allows for the accurate creation of both rural and urban propagation environments. These scenarios can include buildings, walls, trees, variations in surface height, and also include electrical parameters such as permittivitty, conductivity, etc. These 3-D tools have been integrated with a ray-tracing algorithm and the combination allows for accurate simulation of the propagation environment. These models were applied to two mobile propagation scenarios, one at the Lakehurst Navel Air Station in Lakehurst, NJ, and the other in downtown Ann Arbor, Michigan. Figure 18 shows a 3-D rendition of the Lakehurst facility, along with the transmitter location and path of the mobile receiver. Figure 18 shows the path loss, in dB, along the path from Rx01 to Rx75 in the figure. The transmitter is located near the Rx50 location and the frequency of operation is 2 GHz. Both transmitter and receiver are at 2 m height. Figures 4 and 20 show the urban environment and path loss for Ann Arbor, Michigan. The path loss for Figure 20 is determined for the receiver moving from Point A to Point B, in Figure 4 and for tranmitter and receiver heights of 2 and 1.5 m, respectively. The frequency of operation for this simulation is also at 2 GHz.

Figure 17: Lakehurst Propagation Scenario

Figure 18: Path Loss Along Lakehurst Mobile Path

Figure 19: Ann Arbor, MI Propagation Scenario
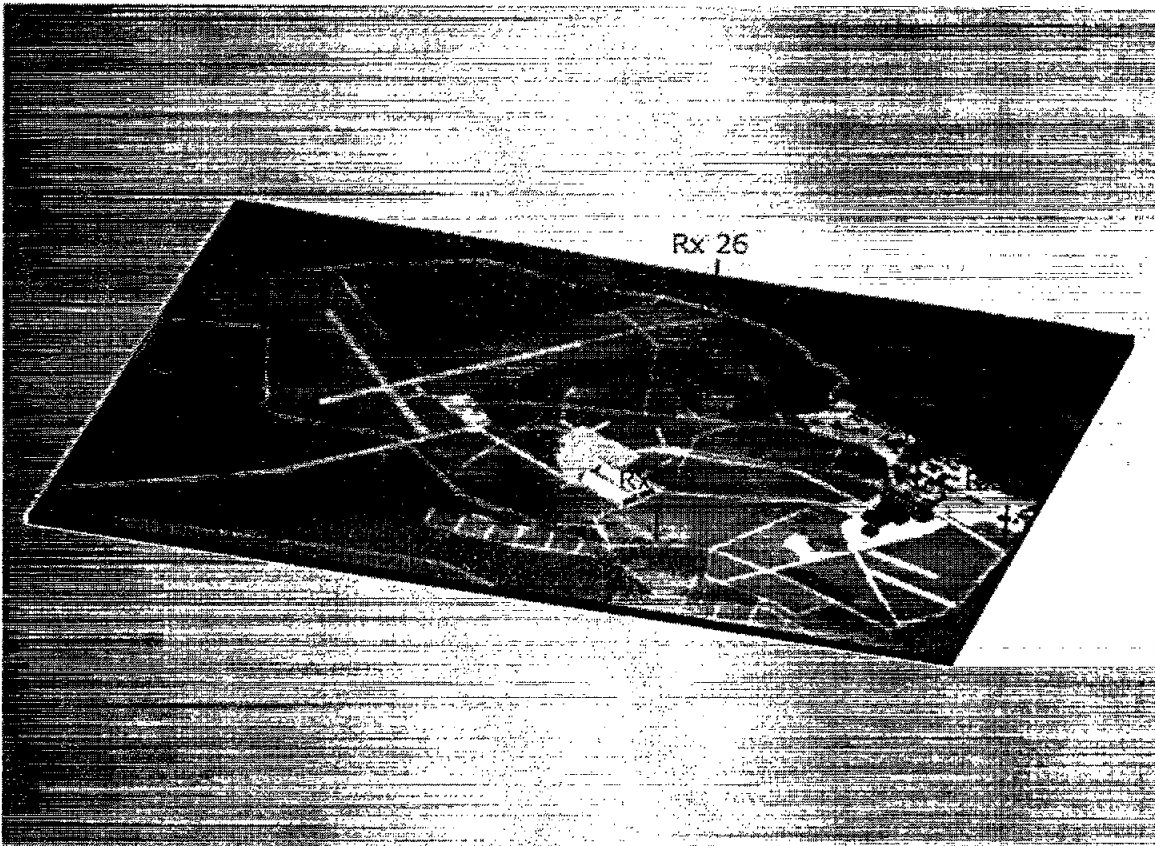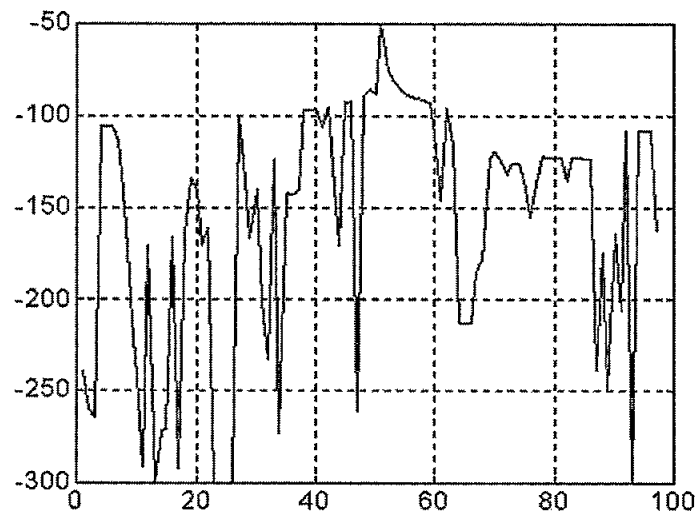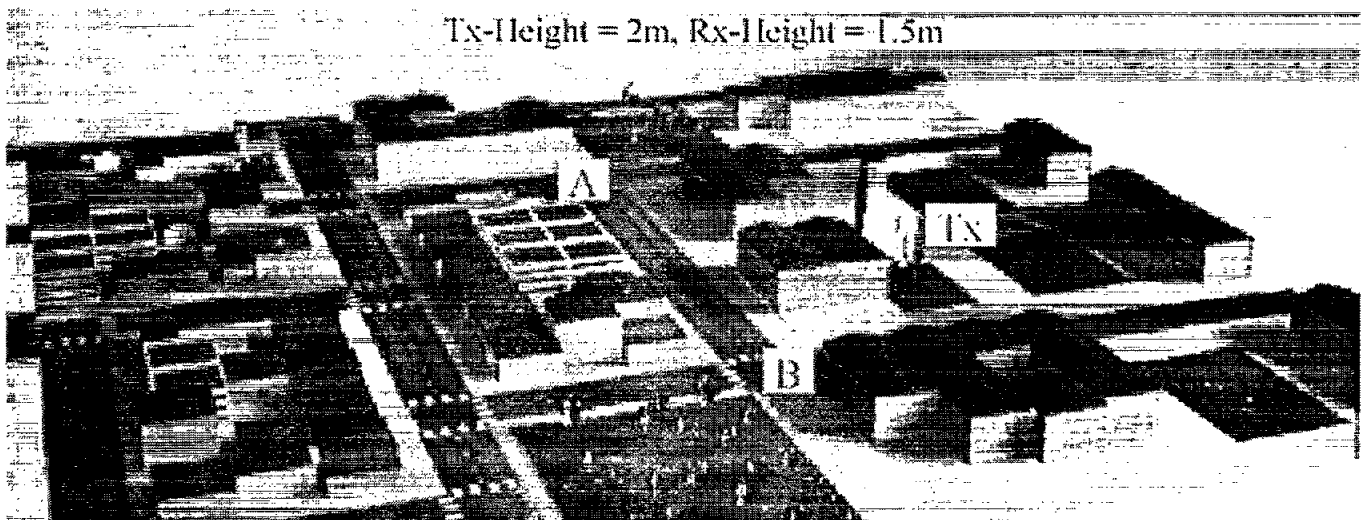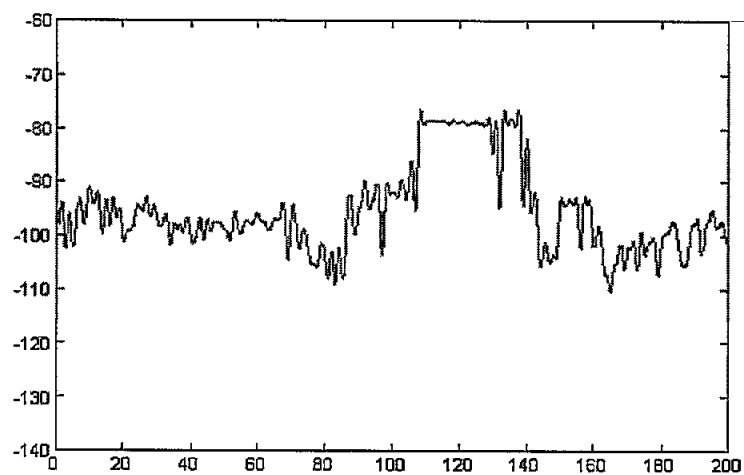
Figure 20: Path Loss Along Ann Arbor Mobile Path

5 Near-surface Propagation Measurements in Forested and Grassy Areas from 400MHz to 35GHz

As part of the continuing effort to characterize wave propagation in a forested environment field measurements were conducted. These measurements were conducted in two different environments, one in a deciduous forest, and for comparison the other in an essentially open area with short grass and coarse, shrub like vegetation. The intent of this preliminary investigation was to gain some insight into both the mechanisms of propagation in a forested environment as well as to begin developing a methodology for controlled measurements in various propagation scenarios. These measurements were conducted when transmitter and receiver were positioned near the ground. This is a scenario used for an unattended network of sensors.

5.1 Measurement Procedure & Set-up

The basic measurement procedure is as follow. The feed points of both the transmit and receive antennas are placed 0.3m above the Earth and data is gathered at ranges of 25, 50, 75, and 100m. Data is gathered from 400MHz to 1GHz, in 100MHz steps, and also at the additional frequencies of 1.35, 1.7, 2, and 35GHz. From 400MHz to 1GHz half-wavelength dipoles are used for the transmit/receive antennas. At 1.35, 1.7, and 2GHz EMCO model 3115 double ridged horns are used, and at 35GHz two Hughes model 45821H-2020 Ka-band standard gain horn antennas are used. Transmit/receive polarization is always vertical. The free-space gain of the dipoles is assumed to be 2.1564 dB (theoretical gain for a half-wavelength dipole) and the gains of the horn antennas are from tabulated data sheets from the manufacturer, and are shown in Table 2. For statistical analysis 10 data samples are taken, at each frequency point, and for each range. The receiver position was fixed and the transmitter moved to provide the data at various ranges and for statistical samples. In what follows, detailed diagrams are provided of both the transmit and receive scenarios for each set of measurements (open area, and forest).

Table 2: Antenna Gain (dB)

Frequency (GHz)	Gain (dB)
1.35	7.7181
1.70	8.3378
2.00	8.4323
3.00	9.1328
35.00	24.00

5.2 Propagation Scenarios

In the following results are presented in terms of path loss. The mean power received in the propagation environment is given in terms of the Friis transmission equation [11] or,

$$< P_r >= \frac{P_t G_t G_r \lambda^2 G_{sys} < PL >}{(4\pi R^2)}, \tag{34}$$

where P_r is the received power, P_t the transmitted power, G_t and G_r the transmit and receive antenna gains, respectively, λ the free space wavelength of the signal, G_{sys} the system active gain (including losses), PL the path loss, and R the distance from transmitter to receiver. In free space the Friis equation is given by

$$P_r = \frac{P_t G_t G_r \lambda^2 G_{sys}}{(4\pi R^2)}. \tag{35}$$

Mean path loss is defined as the ratio of the absolute value of the received power in the propagation environment to that of free space, or the ratio of (34) to (35).

5.2.1 Open Field Scenario

The first set of measurements was made in an essentially open area consisting of a mixture of short grass and shrub like vegetation. From the receiver to 75m there is an approximately 20m drop in ground elevation, which then remains relatively constant out to 100m. Figure 21 shows details of the measurement scenario, with the top of the figure showing a view from above, and the bottom showing a profile of the elevation. Referring to the figure, the dotted lines are indicative of the path along which the 10 statistical samples were taken. As can be seen, at 75m, there is partial blocking of the transmitted signal for some of the data samples, by two trees in the propagation path. The dash-dot line in Figure 21 shows a drop off in ground level (hollow, approximately 10 to 15m deep) across which the 100m measurement was made. At 25m there was essentially no short grass and approximately 30% of the area between transmitter and receiver consisted of the shrub vegetation, approximately 0.5 to 0.6m in height. In transitioning from 25m to 50m the shrub like vegetation was approximately 0.75m in height and covered 100% of the surface with significant short grass cover also. The cover was essentially the same at 75m, and was approximately 0.3m in height. At 100m there was no shrub vegetation however the floor was 100% covered with short green grass, approximately 0.15m in height. Figures 22 through 24 show photos of the open area site. Figure 22 shows an overall view of the transmitter sites, looking from the receive to the transmit points. The two trees which partially block transmission at the 75m site can be seen as well as the gully or hollow in the right of the picture looking out to the 100m site. Figure 23 shows the open area site looking from behind the 75m site and back towards the receiver. Both pictures show clearly the types of vegetation present. In Figure 24 the ground around the receiver can be seen. This was typically ground cover out to the 25m transmit point.

5.2.2 Deciduous Forest

The second set of measurements was made in a deciduous forest, in early autumn, in southeastern Michigan, with the trees still fully foliated and beginning the transition to autumn colors. The ground level transitioned from essentially flat at 25 and 50m to a small hill placing the transmitter approximately 10m above the receiver level, to approximately 15m above receiver level at the 100m range. In close proximately to the receiver were a large tree, approximately 48cm in diameter and 1m distant from the receiver, and what was essentially a single tree with a double trunk, with an overall diameter of 32cm, which was approximately 0.5m from the receiver. All of this can be seen in Figure 30. Again both transmitter and receiver were placed 0.3m above ground level. Figures 25 through Figures 29 show photos of the measurement site in the forest. Figure 25 shows the receiver site, Figure 26 the transmit

Open Measurements

Tree

50m

25m

75m

Rx

Tree

100m

Hollow

≈ 20m   25m

50m

75m   100m
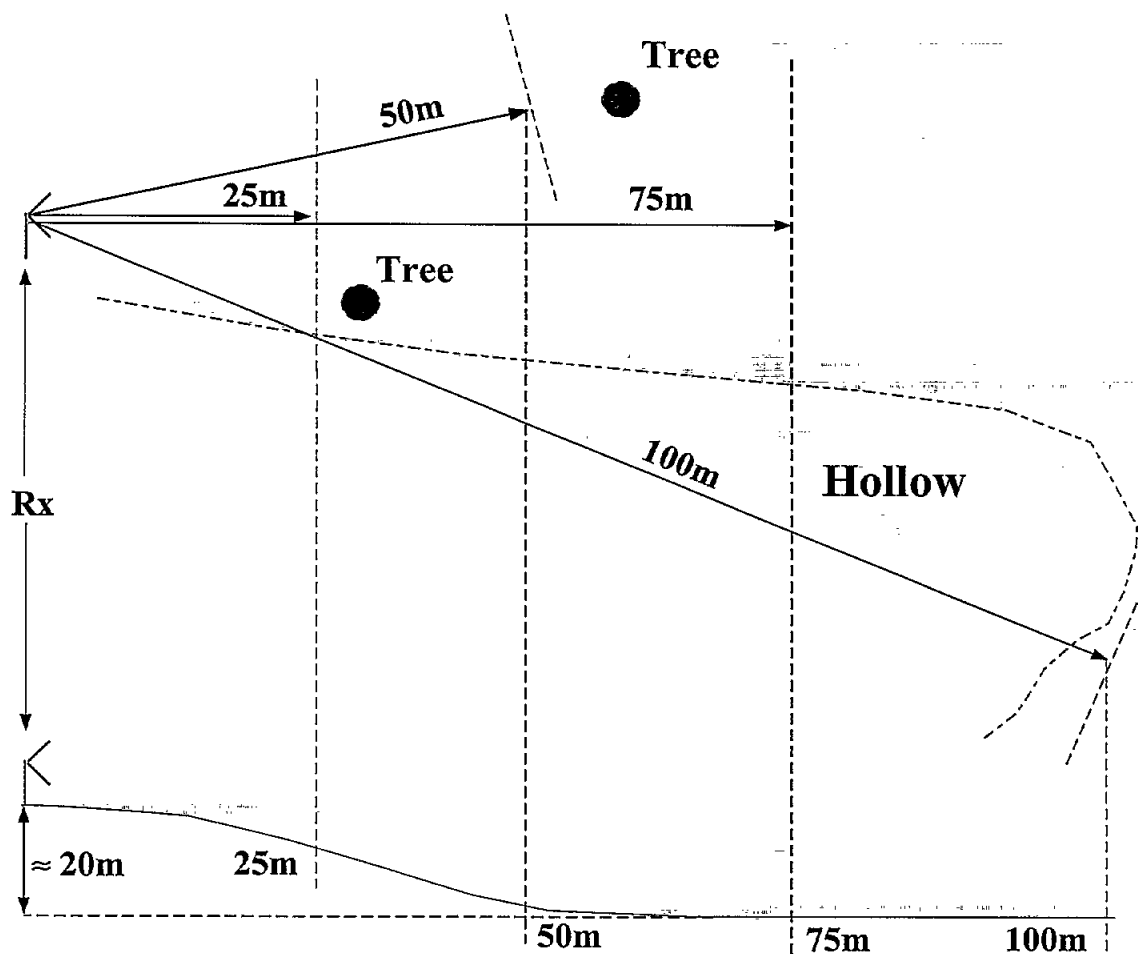
✱ Tx/Rx 0.3m Above Ground Level

Figure 21: Open Area Scenario

area at 25m, Figure 27 the transmit area at 50m, with Figure 28 showing the 75 and 100m transmit sites, looking up from the bottom of the hill that the transmit antenna was placed on. Figure 29 shows a view of a typical part of the forest canopy.

To give some idea of the transmit scenarios in the forest, and since it was not practical for this set of measurements to gather enough ground truth to provide accurate numbers for average tree density, average tree diameter, etc., diagrams of the transmitter sites, for each range in the forest, are shown in Figures 31 through 34. These diagrams show the approximate positions of the tree trunks around the transmitter and the dashed line in each the path the transmitter was moved along, in order to gather the statistical samples. Tree diameters are given in centimeters, with distances to and between trees given in meters. Note that the diagrams are not drawn to scale.

Figure 22: Open Area, Overall View

Figure 23: Open Area, View from Behind 75m Position to Transmitter Site

Figure 24: Open Area, View of Transmitter Area

Figure 25: Transmitter Site, Forested Area

Figure 26: Forested Area, 25m Site

Figure 27: Forested Area, 50m Site

Figure 28: Forested Area, Hilltop View

Figure 29: Forest Canopy

Forest Measurements

1m   1/2m

Rx

17m

10m

100m

75m

25m   50m
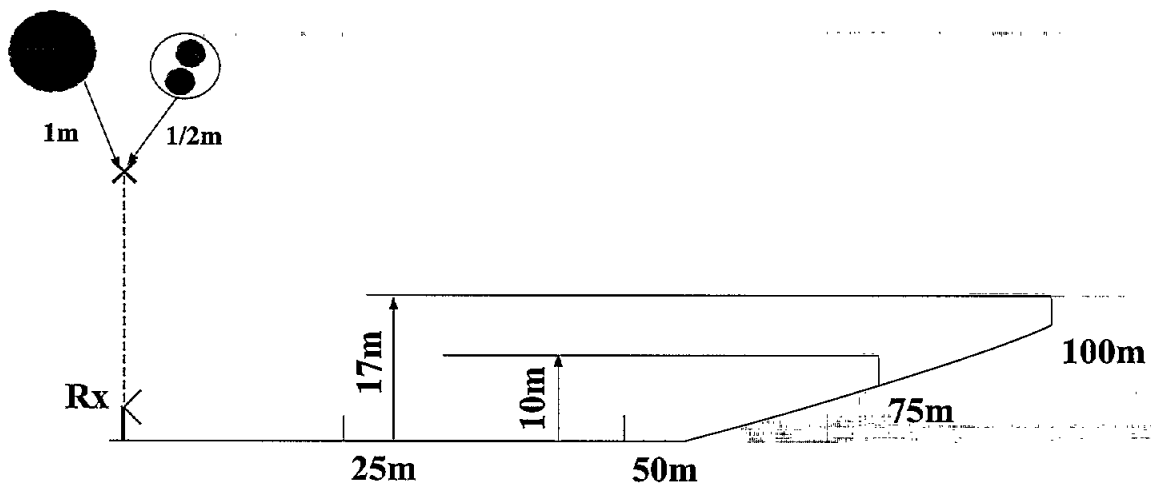
✳ Tx/Rx 0.3m Above Ground Level

Figure 30: Forested Area Scenario

Figure 31: Transmitter Scenario, Forested Area at 25m

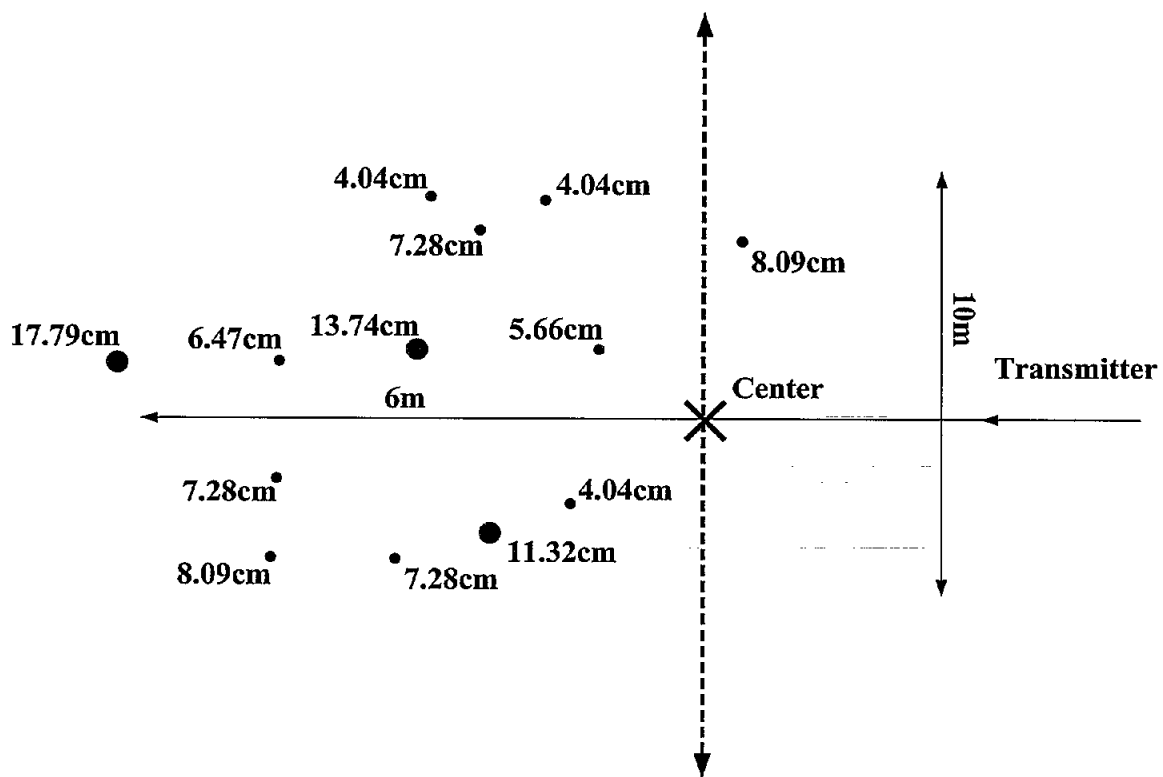Figure 32: Transmitter Scenario, Forested Area at 50m
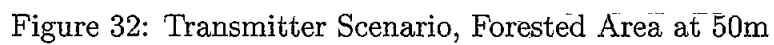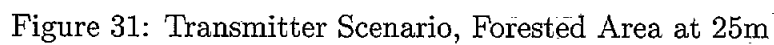
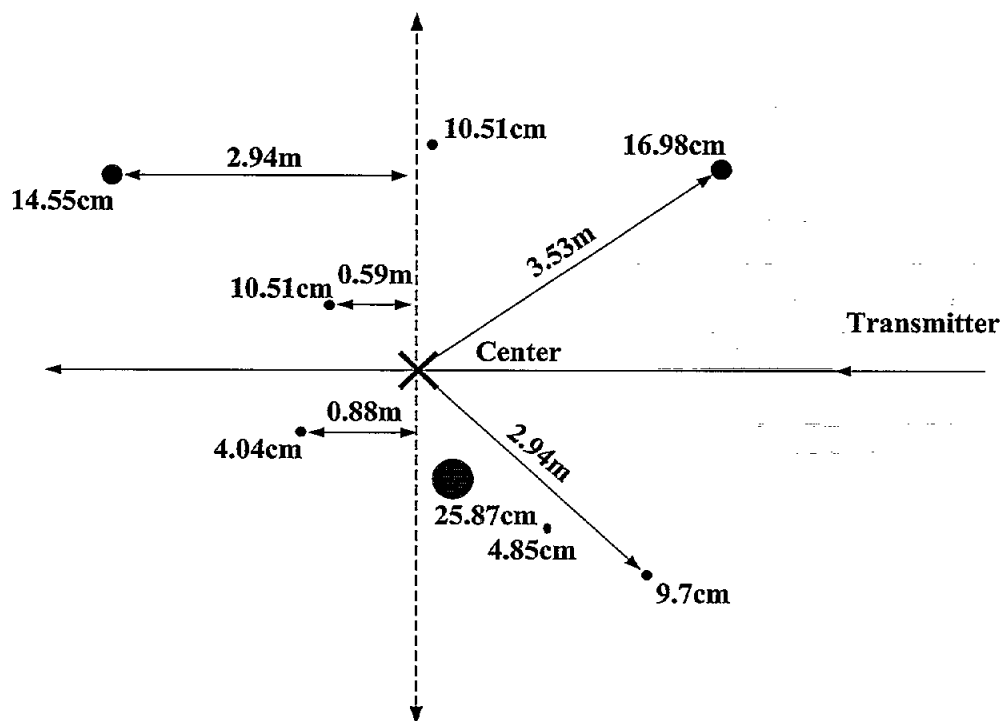Figure 33: Transmitter Scenario, Forested Area at 75m

Figure 34: Transmitter Scenario, Forested Area at 100m

5.3 Results, Low Frequency

In this section results are discussed for the measurements from 400MHz to 3GHz. Ka-band results for both the open and forested area will be presented in a later section.

Figure 37a shows the mean path loss for the open area as a function of frequency and for each range measured, while Figure 38a shows the equivalent results for the forested area. Note that a more negative number in these plots signifies greater path loss.

5.3.1 Open Area

For a dipole operating above a flat impedance surface and and for both source and observation at a fixed height, path loss should increase for increased range to the observation point. Path loss is also a function of the height of the receiver and transmitter. For vertical dipoles very near the surface, the geometrical optics (GO) component of the reflected fields tends to cancel with the direct field and higher order components in the asymptotic field expansion are dominant [12]. These higher order components are usually referred to as a Norton surface wave (NSW) in the literature and for this scenario, the total field power tends to decay at a rate of $1/R^4$. As path loss is normalized to $1/R^2$, in terms of power, the path loss is expected to decay at a rate of $1/R^2$. This decay is based on near cancellation of the direct field with the GO field. If either source or receiver are raised above ground this decay decreases and path loss decreases. Simulated results show that, as a function of frequency the path loss is oscillatory due to the interference between direct and reflected waves, and the frequency of the oscillations increases as source and/or transmitter are raised above the surface. These effects can be seen in Figures 35 and 36. Figure 35 shows the path loss as a function of frequency for fixed antenna and observation heights of 0.3m and for four ranges, 25, 50, 75, and 100m. Figure 36 shows the path loss for a range of 100m, receiver height of 0.3m and varying transmitter heights of 0.3, 1, 5, 10, and 50m.

This basic propagation model would seem to be in contrast to the measured data for the open area path loss, as observed in Figure 37a. As a function of range the path loss appears to be fairly constant, except at low frequencies, (and for a jump when the antennas are changed in going from 1 to 1.35GHz, this will be explained later). As mentioned, for the open area, there is significant surface vegetation, which acts as a diffuse attenuating layer for the reflected fields, and which would effect the reflected fields more at higher frequencies. Therefore it is expected that the path loss would decay as a function of range for low frequencies and become relatively constant at the higher frequencies. This can be observed in Figure 37a. At 400MHz the path loss is seen to become greater with range (except for 100m), while at higher frequencies the curves tend to come together. Data for the 100m curve is taken over the hollow, seen in Figure 21, where there is no reflected field component and therefore no degree of cancellation with the direct field, and thus this curve has a higher level (lower path loss) when compared with the others.

Note that in Figure 37a there is a significant jump in the measured path loss (less path loss) from 1 to 1.35GHz. Recall that in transitioning from 1 to 1.35GHz a more directive, ridged horn antenna, replaces the half-wavelength dipole. This more directive antenna tends to minimize the ground reflections and therefore minimize cancellation of the reflected and direct fields.

In Figure 37a it is also observed that the path loss in the open environment is basically independent of frequency (accounting for the jump from 1 to 1.35GHz and recognizing the effect of statistical error). From the basic propagation model shown previously, it is expected
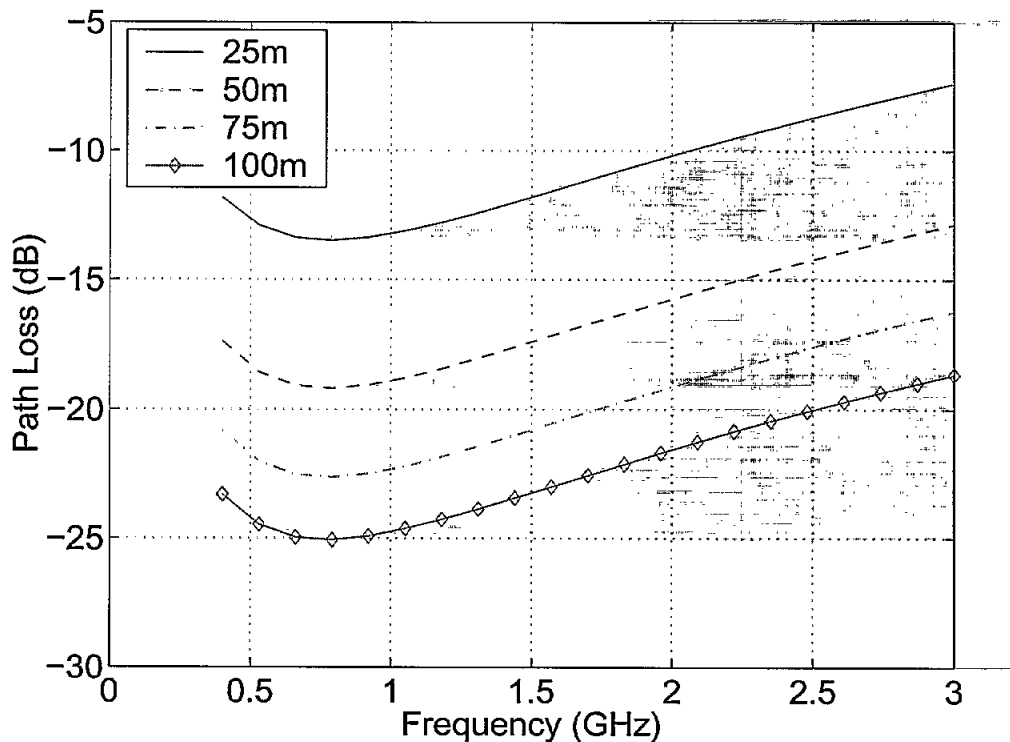
Figure 35: Total electric fields above a flat impedance surface. Transmitter and receiver @ 0.3m height, for ranges of 25, 50, 75, and 100m. Soil is San Antonio gray clay Loam with a density of 1.4 g/cm^3 and 20% gravimetric moisture content

to see a change over frequency due to the interference of the direct and reflected waves, however as discussed in the previous paragraph this effect is minimized due to the effect of the vegetation on the reflected wave.

5.3.2 Forested Area

The mean path loss in the forested environment, from 400MHz to 3GHz, is shown in Figure 38a. Ground reflections in the forest tend to be insignificant and the main cause of path loss is from the highly scattering media of the trunks as well as attenuation through foliage at the higher frequencies measured. It is therefore expected that the path loss as a function of range will be greater. This is the case in Figure 38a in going from 25 to 50m, however the curves for 50, 75, and 100m tend to about the same levels as a function of range. This can be explained by remembering that in the forest the measurements at 75 and 100m were at an elevated position, on a hill side (see Figure 30). As the transmitter was placed higher on the hill, the transmit/receive path tended to travel through higher parts of the tree structure (smaller branches) and thus experienced less attenuation. Also at 25 and 50m, with the antennas placed so closely to the ground, ground clutter, in the form of dead and fallen branches and tree trunks had a more significant effect on the signal.

In Figure 38a, except for the 25m curve, there is no jump in level observed, when the dipole antennas are replaced with the ridged horns above 1GHz. Since as mentioned, the reflected fields have little effect in the forest this is expected, remembering that the jump in levels in the open area in this region was due to the more directive nature of the horn antennas, and therefore less ground cancellation. As for the 25m curve, most of the statistical
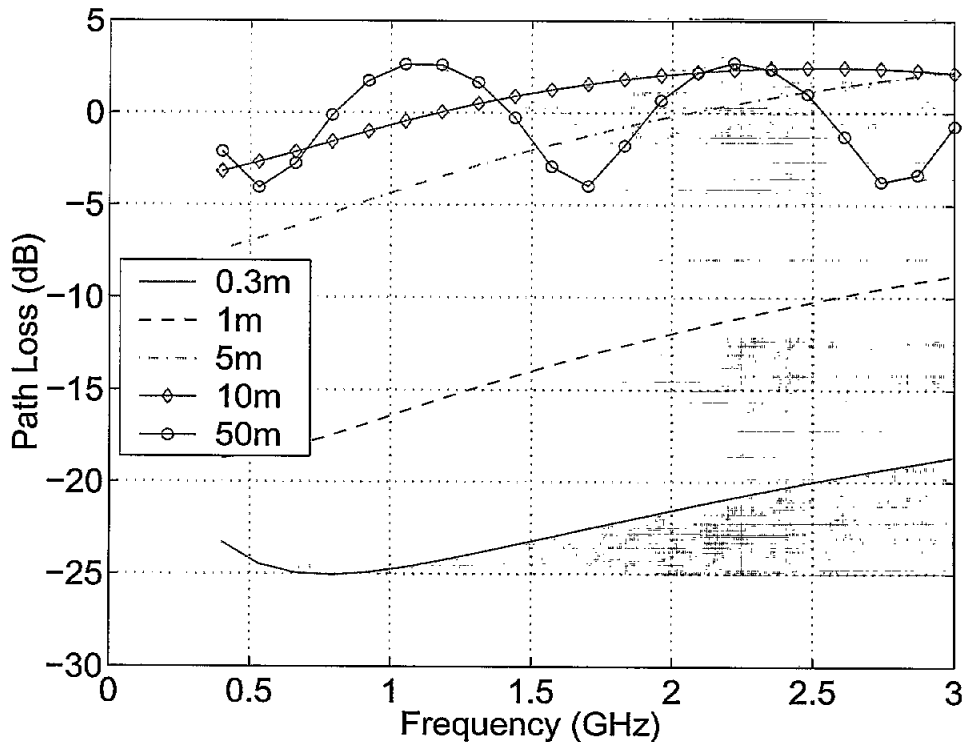
Figure 36: Total electric fields above a flat impedance surface. Receiver @ 0.3m height, range is fixed at 100m, for transmitter heights of 0.3, 1, 5, 10, and 50m. Soil is San Antonio gray clay Loam with a density of 1.4 g/cm^3 and 20% gravimetric moisture content

samples taken had partial line of sight (LOS) transmission and it is possible, at such a short range, that a coherent multipath component was introduced by the broad beam of the dipole antennas, which again tended to cancel with the incident field.

It would be expected that in the forest environment the path loss as a function of frequency would increase, for higher frequencies. This is not the case, however when looking at Figure 37a.

In Figure 37b and Figure 38b the standard deviation for the open and forested area, respectively, are shown. It is observed in both plots that the trend over both range and frequency are very similar to that of the mean path loss. This is expected, as the ratio of the mean path loss to standard deviation should be constant in both the open and forested environment. This can be seen in Figures 37c and 38c where this ratio is plotted for the open and forested areas, respectively.

A final question at low frequencies is why the levels of the mean path loss in both the open and forest areas are similar. It would normally be expected that the path loss in the forest would be greater, however it would seem that for this scenario of transmitter and receiver very near the ground that the cancellation of the direct and GO fields in the open area produces similar attenuation in the total fields, as does the effect of the highly scattering environment in the forest. This conclusion is supported by the fact that in the frequency range where the ridged horn is used, and ground reflections are minimized, that the levels of mean path loss are consistently less for the open area when compared to the forest data.

49
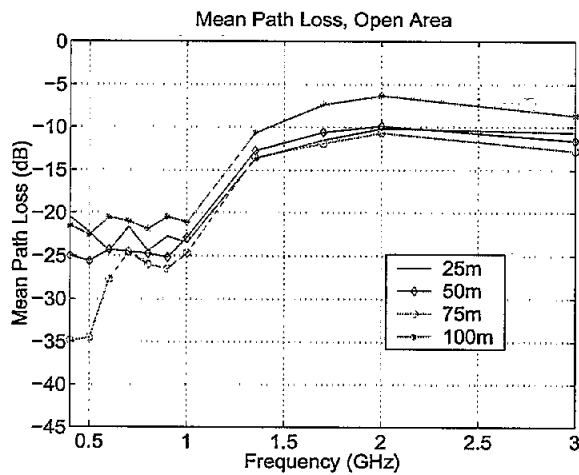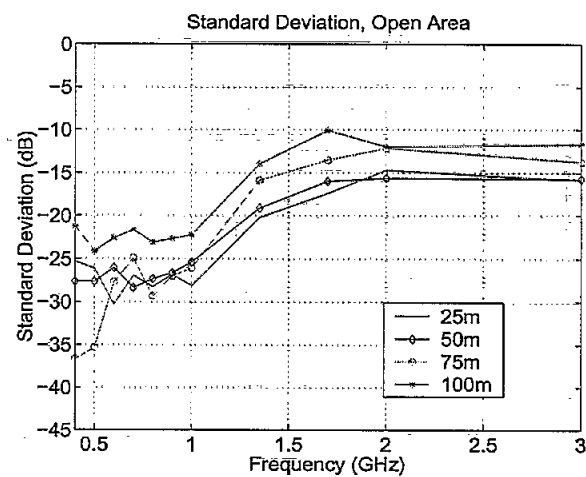
(a) Mean Path Loss

(b) Standard Deviation
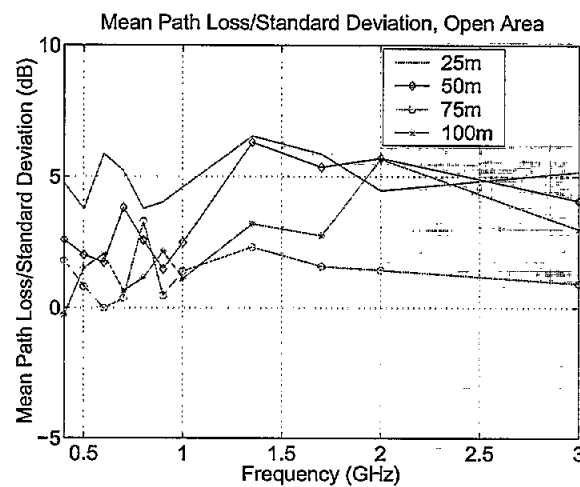
(c) Mean Path Loss/Standard Deviation

Figure 37: Open Area Measured Results, Low Frequency
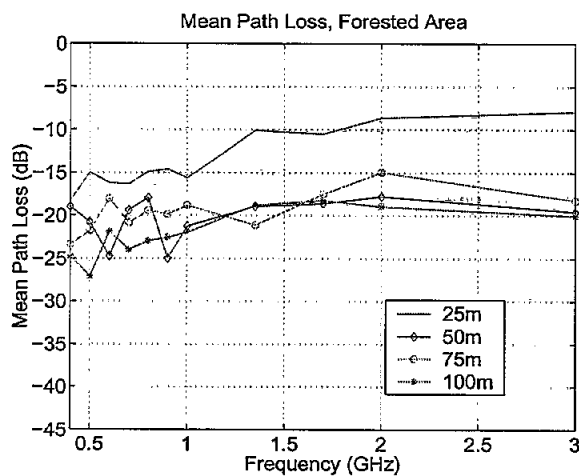
(a) Mean Path Loss
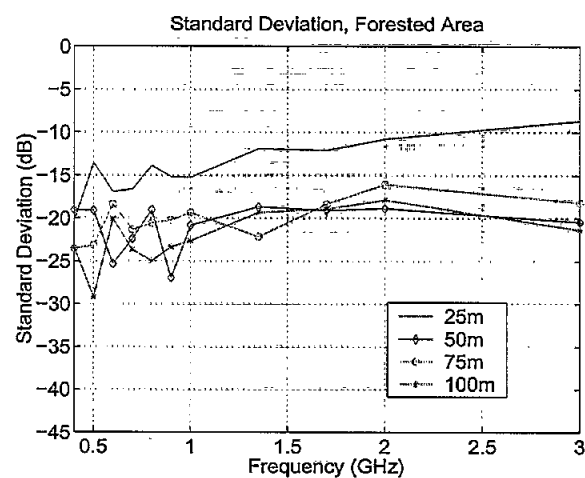
(b) Standard Deviation
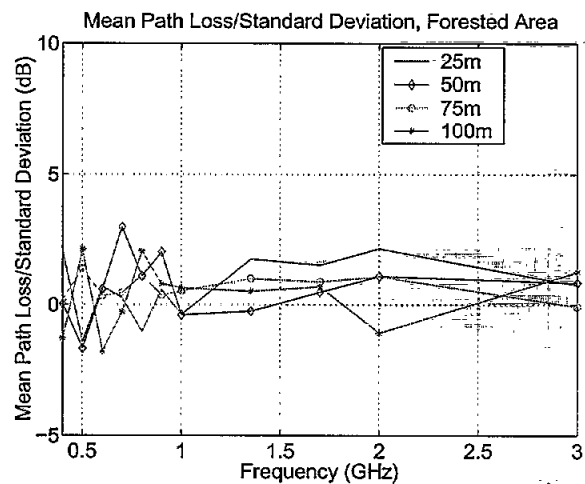
(c) Mean Path Loss/Standard Deviation

Figure 38: Forested Area Measured Results, Low Frequency

5.4 Results, Ka-band

In this section results from the Ka-band measurements in both the open and forested environments will be observed and analyzed. Figures 39a and 39b show the mean path loss and standard deviation, respectively, as a function of range for a 35GHz signal, with Figure 39c showing the ratio of the mean path loss to standard deviation at 35GHz. At this frequency ground reflections in the open area are insignificant and in the forest, even for the higher elevation of the transmitter at 75 and 100m, attenuation is significant. It is therefore expected that the signals in both areas as a function of range will decay and that the path loss in the forest will be greater. In observing Figure 39 the signal in the forested area behaves as expected. The path loss for the open area at 25 and 50m does not, however. It would be expected that at close range (25m), and due to the absence of an incoherent reflected field, that the path loss would be close to 0 dB and that the path loss curve would decay exponentially as range increased. Also the path loss in the open area should be less than that in the forest. A possible explanation for the data at 25 and 50m is that LOS was blocked for these ranges by the shrub vegetation and the height difference between transmitter and receiver, while at 75m many of the samples had LOS transmission, and as mentioned the 100m was a LOS transmission. This vegetation would have a much more significant effect at Ka-band than at lower frequencies and could account for the discrepancies seen in the shorter ranges.

As before the standard deviation curves are of similar form to the path loss, and the ratio of mean path loss to standard deviation is fairly constant, as expected. This can be seen in Figures 39b and 39c.
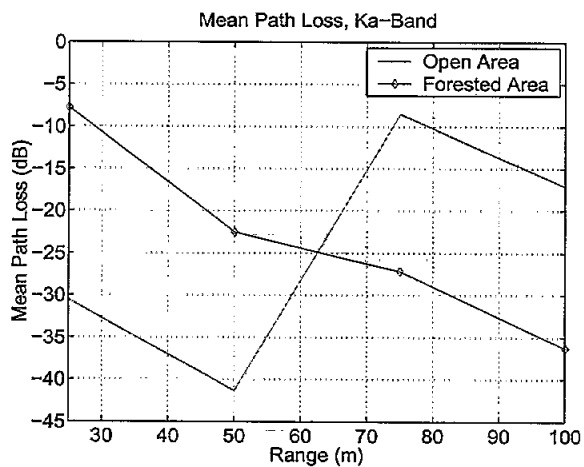
(a) Mean Path Loss
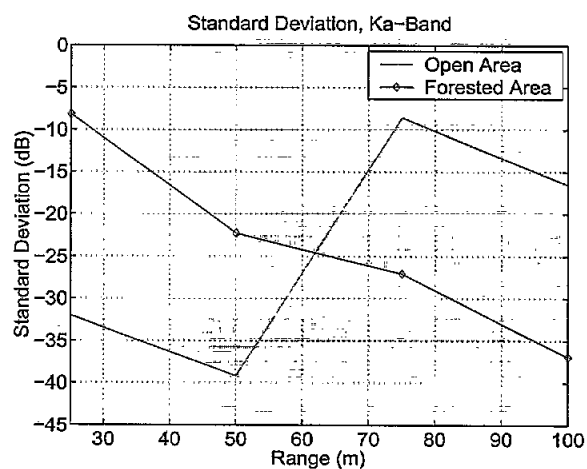
(b) Standard Deviation
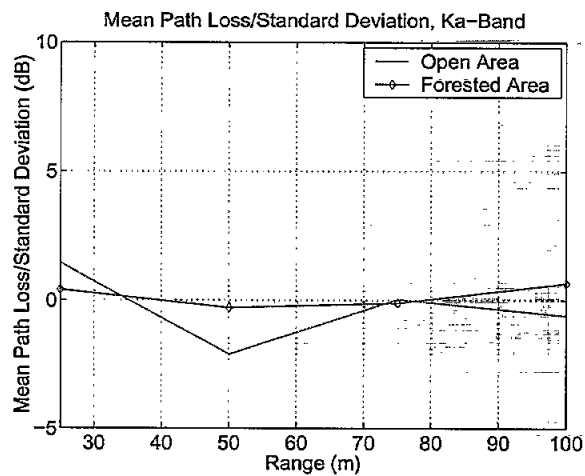
(c) Mean Path Loss/Standard Deviation

Figure 39: Measured Results, Ka-Band

5.5 Conclusions

In this section results from experimental measurements in an open and forested environment were presented and analyzed. The intent of the experiment was to provide some preliminary insight into propagation in a forested environment and also to establish a methodology for future experiment. While in general the measurements could be explained in a reasonable way, there were several anomalies and more investigation is needed to correlate theoretical models with the measurements. Also more extensive, controlled measurements, in various propagation environments, need be performed in the future.

6 A Measurement System for Ultra Wideband Communication Channel Characterization

6.1 Introduction

In order to assess the performance of any communication system it is necessary to characterize the communication channel. Channel characterization can be done in two ways: 1) experimentally and 2) by computer simulation. Some of the more commonly used attenuation models are heuristic, based on measured data [13, 14], and in some cases overly simplified electromagnetic formulations [15], with little correlation to the physics of the problem. Thus, while simple to implement, these models lack the desired accuracy and generality.

In recent years significant efforts have been devoted towards the development of physics-based electromagnetic (EM) models, which apply analytic and numeric techniques for channel modeling [16, 17, 18, 19, 2, 20, 21, 22, 23, 24]. These models allow for characterization of the communications channel to a high degree of fidelity, and are able to simulate varied propagation environments, including the polarimetric aspects of the channel.

Despite significant progress in this area, experimental characterization of a communications channel is still necessary for gaining insight into the mechanisms of wave propagation as well as for the validation of computer models. Past experimental work on channel characterization has been carried out often over limited bandwidths [25, 26, 27, 28, 29, 30], and at times for specific systems such as AMPS and PCS wireless communication systems [31]. In these experimental efforts, limited channel characteristics such as path loss and fading statistics have been determined. Although channel characterization over a narrow bandwidth is straight forward, measurements over a wider bandwidth, and coherently, is significantly more complex. Basically, the problem stems from the fact that coherent receivers with a wide bandwidth allow significant noise power to enter the receiver, which limits the system's dynamic range. Measurement systems employing a single vector network analyzer have been proposed for indoor channel characterization efforts [32, 33, 34, 35]. With this approach, coherent, wideband, propagation measurements can be performed over relatively short distances. To maintain coherence, the signal generated by the network analyzer is relayed to the distant transmitter via long RF cables or optical links [35]. While this approach performs well in an indoor setting, it is impractical for an outdoor setting where multiple sites need to be accessed, often behind significant foliage. To circumvent this problem a novel approach, based on a stepped frequency technique is developed. The system uses two vector network analyzers (VNAs), one as a transmitter and one as a receiver and is synchronized in frequency step by using two rubidium atomic clocks. The sensitivity of the receiver is determined by the intermediate frequency (IF) filter internal to the VNA which can be set a low as 3 Hz. The combination of the narrowband IF filter and the synchronized frequency sweep allows for a highly sensitive measurement system, and operation over a very wide bandwidth, in principle limited by the antennas and the specific VNAs used. In Section 6.2, the design and operating principles of the system will be discussed, while in Section 6.3 results from a measurement campaign, conducted at the Lakehurst Naval Air Station, in Lakehurst, New Jersey, are presented and analyzed, including techniques used for post processing the data and extracting the attenuation characteristics of the channel, as well as it's frequency decorrelation.

6.2 Wideband Measurement System

A VNA is a microwave measurement instrument capable of measuring both the amplitude and phase of the reflection and/or transmission coefficients of the device under test (DUT). In addition to different processing and calibration units, any VNA has a microwave signal generator, which can be either in the form of an analog sweeper or a synthesized source, and a number of built in, high performance vector receivers capable of measuring both the amplitude and phase of the input signal. The microwave sweeper allows for rapid acquisition of the signal in broadband measurements, and also provides a constant output power over the entire frequency band. For accurate phase measurements, the receiver uses a phase lock loop (PLL) and either an internal or an external source as a reference signal for the PLL. Most VNAs such as the HP8753D or HP8720D have the option to use an external continuous wave (CW) reference (usually a 10 MHz sinusoidal wave). This allows the user to select a highly stable CW signal as a frequency reference, in order to achieve high phase accuracy.

A communication channel can be viewed as a two port passive device with input and output ports located at the transmitter and receiver respectively. The advantage of using a VNA as the transceiver is its stepped frequency mode of operation, and it's inherent ability to sweep over a wide frequency band (50 MHz - 20 GHz for an HP8720D) while maintaining a high receiver sensitivity. To maximize receiver sensitivity the receiver bandwidth (IF filter) can be set as low as 3 Hz while sweeping through a wide frequency band. This allows for coherent measurements (magnitude and phase) of very weak signals over a wide dynamic range. Unlike most two port devices however, the ports of this system are distant from each other and in order to perform transmission (S_{21}) measurements it is necessary to employ two VNAs, one as a transmitter (Tx) and one as a receiver (Rx). In addition, amplifiers, antennas, filters and data acquisition systems are also needed. The difficulty of this type of disconnected system is in providing a common, stable reference to the PLLs of both VNAs, and also in synchronizing their respective frequency sweeps. Both of these difficulties are solved by using two identical, highly-stable, and synchronized Rubidium Atomic Clocks (RbAC) [36]. Synchronization of these clocks is accomplished by simply connecting their time reference outputs together, and once synchronized they each provide what is essentially a common, and highly stable 10 MHz frequency reference and a 1 pulse per second (PPS) system clock (which synchronizes the respective frequency sweeps), for each VNA. The short term and long term stability of these atomic clocks are, respectively, $1 \times 10^{-12}/10$ sec and $5 \times 10^{-10}/$year.

In order to measure the channel response correctly both the transmitter and the receiver must synchronously sweep through the frequency band, with the allowed timing error within $\pm$ the 3 dB bandwidth of the receiver IF filter, around the frequency being measured (Note that for large propagation delays, which cause a timing error outside this allowed range, a delay can be introduced in the timing of the receiver RbAC, to account for this. This delay is controlled by the serial port line to the data acquisition computer, shown in the system block diagram in Figure 40. In results shown later however, distances of up to 1.1 Km were measured, with out a need for any timing adjustments to the receiver clock). The atomic clocks could be used to trigger each sweep through the frequency band, and the VNAs allowed to then independently sweep through the band. There is however, sufficient difference in the nominal sweep times of each independent VNA, even when set to be identical, to cause the system to loose synchronization. Therefore the atomic clocks are used to move each VNA, step by step, through each discrete frequency point to be measured in the band. This is accomplished by operating the VNAs in the "External Trigger On Point" mode. In this

Figure 40: Block diagram of the Propagation Measurement System.

mode an external trigger is required, at the "EXT TRIG" input of the VNAs, to step the network analyzers to through each discreet frequency point in the measurement band. This can be seen in Figure 40, which shows a block diagram of the measurement system. To implement this for both the Tx and Rx VNAs, and referring to Figure 40, the 1 PPS output of the rubidium atomic clock is used as a system clock, which is then fed to a digital counter that creates a time reference (by dividing it by 16) which is used to set the period of the frequency sweep (16 s). This time reference in turn signals a function generator to send a burst of N trigger pulses to the "EXT TRIG" port of the VNA with the rate of ν pulse per second (where N is the total number of frequency points). Thus, a frequency sweep is performed in $t = N/\nu$ seconds. The sweep can be performed over a continuous frequency band, or the VNAs can be programmed to operate at discrete sub-bands, with non-uniform frequency sampling. This is particularly useful for conducting measurements in places where transmission over certain frequency bands or at certain frequencies with in the measurement band are not allowed, for example near or in airports, military bases, etc.

Figure 41 shows the flowchart of the system operation. To summarize system set-up and operation, and referring to Figure 41, the first step is to synchronize the 1 PPS outputs of the transmitter and receivers of the RbACs so that the Tx/Rx time references are the same. This can be done simply by feeding the 1 PPS output of one of the clocks to the synchronization input of the other one [36]. Every 16 second the function generator receives a trigger signal from the digital counter and sends a burst of N pulses (TTL compatible) to the VNA with the rate of ν PPS. These are the trigger signals, denoted "trigger" in Figure 41, which causes the transmitter VNA to start stepping through the desired frequency band. The same thing happens simultaneously at the receiver end, except that the receiver VNA begins to receive the signal that has been transmitted by the Tx VNA. After each frequency sweep the Tx/Rx computers acquire the measured data for post processing. In order to ensure that a new sweep does not begin while this data acquisition (DAQ in Figure 41) is in progress, both VNAs are operated in single sweep, as opposed to continuous sweep, modes. This mode requires that each VNA be armed by the DAQ computer, before they will accept any trigger signal for a frequency sweep, thereby allowing the DAQ computer to hold the
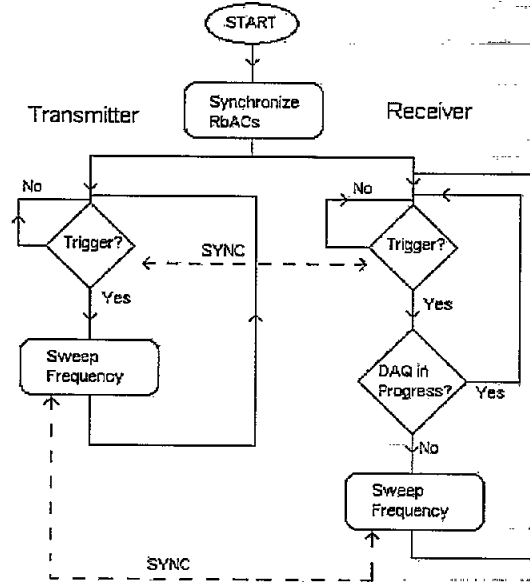
57

measurement cycle, while DAQ is in progress.

Figure 41: Flow chart of the system operation.

6.2.1 Calibration, and Operation

The received signal power can be obtained using the modified Friis transmission formula:

$$P_R = \frac{P_T G_T G_R}{L_{FS} L_A} \tag{36}$$

where P_T, G_T, and G_R, are the transmitted power, and the antenna gains of the transmitter and receiver, respectively, L_{FS} is the free space loss and L_A is the additional path loss in the channel. The noise power at the input of the receiver VNA is calculated using:

$$N_R = KTB_{IF} \tag{37}$$

where K is Boltzman's constant, B_{IF} is the IF bandwidth of the VNA that can be set by the user. For the case of HP8753D this bandwidth can vary from 3 Hz to 3.7 kHz. In (37) T is the equivalent noise temperature of the system including the antenna noise temperature. A desired received signal-to-noise ratio, defined as $SNR_R = P_R/N_R$, determines system compatibility in the path loss measurements. For most practical purposes a SNR_R of 15 dB is sufficient for accurately determining the statistical behavior of the channel. Referring to (37), noise power is effected by both the system bandwidth, set by the IF bandwidth of the receiver, and by the equivalent noise temperature, T, which is usually determined by the noise figure (NF), of the first receiver amplifier, or pre-amplifier. Therefore, the system SNR_R can be significantly reduced by reducing the IF bandwidth of the receiver VNA, but as a result of this the sweep time and the overall measurement time is increased. Hence depending on the output power, distance, expected path loss etc., there is tradeoff between the IF bandwidth, sweep time, which determines the speed at which measurements can be taken, and the desired SNR_R. Taking this into account, the IF bandwidth for the system

was set to 3 kHz. This in combination with a low-noise pre-amplifier (LNA), with a NF of 1.5 dB and a gain of 27 dB, resulted in a noise floor for the receiver of -90 dBm. In addition, due to the long distances over which this measurement system will be applied, high power radio frequency (RF) amplifiers were used to amplify the transmitted signal.

To perform measurements over a wide frequency band, it is necessary to use either a very wide-band antenna, or to use different antennas for measuring different sub-bands. The gain and radiation characteristics of the antenna(s) used in the system as well as the frequency responses of the power amplifier, LNA and cables used, should be measured over the entire frequency band so that their effect can be calibrated out. Two different methods for calibration of the system are used. In the first method all of the system components' (cables, amplifiers, etc), gains and losses are characterized individually using the VNA and then effects are accounted for in the calibration process. In the second method, which is illustrated in Figure 42, the output of the power amplifier is connected to the input of the LNA via a high power calibrated attenuator and the overall transmission coefficient (S_{21}), without the interlying propagation medium, is determined. In this approach all components except the antennas, are characterized and the method has the advantage of calibrating out the effects of connector losses and mismatches. The antennas used in this system are calibrated standard gain antennas with linear polarization and relatively low gains (wide beam). As is true for most wideband antennas the location of the phase center of the antenna changes with frequency but the change is less than the extent of the antenna structure. This dispersive behavior of the antenna can cause spectral decorrelation to some extent but it is much lower than what is caused by the channel, and can therefore be ignored.
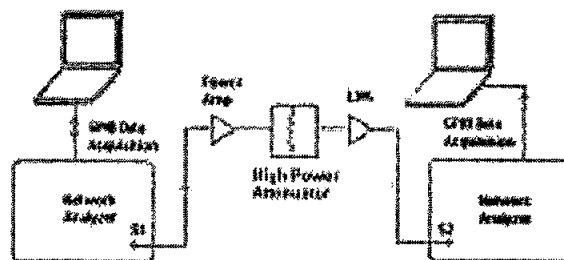

Figure 42: Block diagram of the calibration set-up of the system.

6.3 Measurement Campaign at Lakehurst

In this section a measurements campaign, using the coherent propagation measurement system and conducted at the Lakehurst Navel Air Station, Lakehurst, New Jersey, will be described. Results will be shown, including system performance specifications, mean path loss (PL) in terms of power, and frequency coherence analysis.

6.3.1 Measurement Parameters

The measurements at Lakehurst were performed in the 30 MHz to 3 GHz range in three sub-bands, 30 MHz to 200 MHz (defined as Band 1), 200 MHz to 1 GHz (defined as Band 2), and 1 to 3 GHz (defined as Band 3). These restricted spectrums were limited by the authorities at the Lakehurst base and shows the system's capability to operate in arbitrary sub-bands within the system bandwidth. A 10 W power amplifier, Amplifier Research (AR)

model 10W1000, was used for the transmission of frequencies at and below 1 GHz, and a 30 W amplifier, AR model 30S1G3, was used for transmission in the 1 to 3 GHz band. For efficient transmission, different antennas were used in each sub-band. EMCO bowtie antennas, models 3109 (rated at 2 KW continuous wave (CW) power) and 93110B (from HP) were used for the transmit and receive antennas in Band 1, respectively. EMCO models 3148 and 93146 (also from HP) log-periodic antennas were used for Band 2, and two EMCO model 3115 horn antennas for Band 3. Due to transmission restrictions at Lakehurst, the transmissions frequencies were limited to specific frequencies and bandwidths within each sub-band. Table 3 lists the allowed transmission frequencies in terms of center frequency, f_0, and bandwidth, BW, for each allowed transmission band (Note that within the ranges specified in Table 3 transmission frequencies were at discreet 1 MHz intervals).

Table 3: Allowed transmission frequencies at the Lakehurst base in terms of center frequency f_0, and bandwidth, BW. Frequencies are transmitted at discreet 1 MHz intervals across each range specified.

Band 1: 30 MHz to 200 MHz		Band 2: 200 MHz to 1 GHz		Band 3: 1 GHz to 3 GHz	
f_0 (MHz)	BW (MHz)	f_0 (MHz)	BW (MHz)	f_0 (MHz)	BW (MHz)
38	16	325	10	1747	32
70	16	350	32	1872	32
–	–	390	32	2440	46
–	–	435	25	2550	10
–	–	493	46	–	–
–	–	524	8	–	–
–	–	561	8	–	–
–	–	600	8	–	–
–	–	641	8	–	–
–	–	670	48	–	–
–	–	806	8	–	–
–	–	915	46	–	–

6.3.2 Measurement Results

Before beginning an analysis of the measured data taken at the Lakehurst site, it is important to note the capabilities of the coherent measurement system. Figure 43 shows an example of the dynamic range of the measurable propagation loss between the transmitter and receiver for the system, through the entire range that measurements were taken. This is essentially a measure of system sensitivity, and can be improved by further narrowing the IF bandwidth of the receiver. To determine this maximum measurable propagation loss, the receiver signal is sampled, with no transmitter signal present, and normalized to the transmitter power, i.e., Figure 43 shows the receiver noise power (including the LNA pre-amplifier), referenced to the transmitter power. The IF bandwidth of the receiver NWA is set at 3 KHz, but can be set as low as 3 Hz, to further improve system sensitivity. Figure 43 is normalized, assuming a transmitter power of 10 W. In Figure 43, data was taken at each frequency point in the measurement band. The change in power levels observed across the band are typical of noise
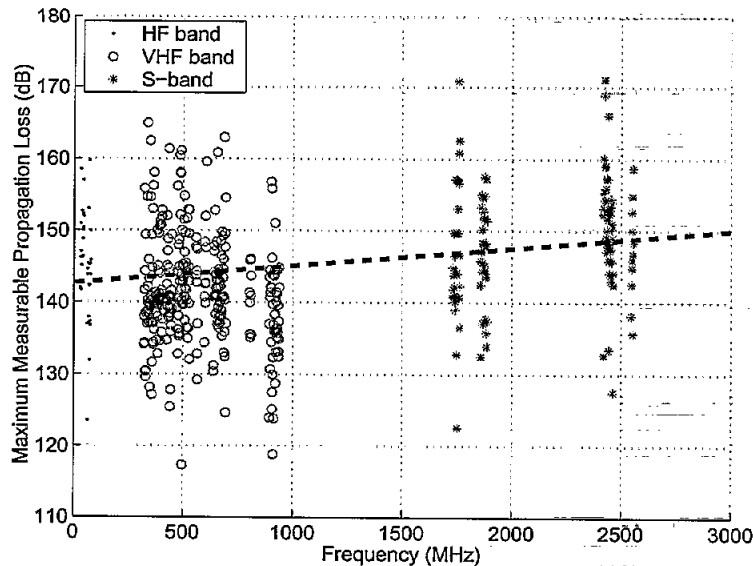
Figure 43: Measurable propagation loss of the system.

power fluctuations in a measurement system. The dashed line in the figure is a best fit curve, which is provided as a reference. As can be seen in this figure, the dynamic range of the measurable propagation loss across the measurement band is in excess of 115 dB, for the IF band setting of 3 KHz.

For all measured results shown, the transmitter was at a fixed location, with data from two receive sites provided here. At each receiver location, approximately 100 spatial samples were taken on a line perpendicular to the line between transmitter and receiver. For each sub-band the spatial samples were taken over a range of $50\,\lambda$ at the lowest frequency in the sub-band, in order to capture the effects of slow fading. To capture the effects of fast fading, the sampling increments began at $1/2\,\lambda$ increments at the highest frequency in the sub-band, gradually increasing to $1/2\,\lambda$ at the lowest frequency sub-band.

The forested areas at the Lakehurst site consisted mainly of pitch pine, with some interlying short vegetation. The pine trees had an average tree density of 0.113 Trees/m^2, average height of 9 m, average crown depth of 5 m, and an average trunk diameter of 16 cm.

The left side of Figure 44. shows an ariel view of the Lakehurst site. On the right side of Figure 44, the transmitter location, along with the two receive sites, is pictured. The transmitter site is located at the bottom of the photo, and is marked as Tx. The receive sites, designated Rx1 and Rx2 in Figure 44, are located vertically from the Tx site, at distances of approximately 490, and 1120 m, respectively. Note that the area between the Tx and Rx1 is clear of forest, while the interlying area between Rx1 and Rx2 consists of approximately 100 m of clear area, and 530 m of forest, with Rx1 located at approximately 100 m from the forest, and Rx2 located on the back side of the forest, within 2 m of the forest. The transmitter and receiver at all locations, and for all bands measured is set at 2 m height. Unmarked areas are clear of forest, and may include some short vegetation.

In order to isolate the effects of the forest on PL, the measured data taken at Rx2, is normalized to that taken at Rx1. Figure 45a shows the measurement scenario, with Figure 45b showing the PL at Rx2, referenced to that at Rx1. The received power P_r,
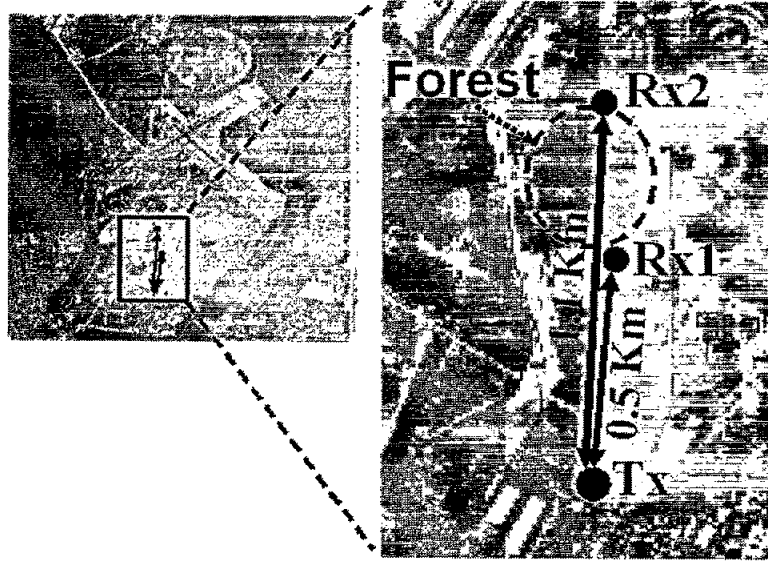
61

Figure 44: Lakehurst measurement site.

referenced to the transmitter power P_t, is given by:

$$\frac{P_r}{P_t} = \frac{(G_t G_r)^2}{(4R^2)} \frac{1}{R^m} PL,$$ (38)

where $G_t G_r$ are the transmit and receive antenna gains, respectively, R is the distance between transmitter and receiver, PL is the PL of the forest, and m is an attenuation factor caused by the ground effect. Note that the first factor in (38) corresponds to the free space PL, as previously given. This ground effect can vary from 0 for a very rough ground, to 2, for cases of transmit and receive antennas very close to a perfectly flat earth. If R_1 and R_2 are the distances to Rx1 and Rx2 respectively, the power received at Rx2 referenced to that received at Rx1 is given by:

$$\frac{P_{r2}}{P_{r1}} = \left(\frac{R_1}{R_2}\right)^{m+2} PL_{forest} = \left(\frac{490}{1120}\right)^{m+2} PL_{forest},$$ (39)

where PL_{forest} is the effects of the foliage on PL.

Referring to (39), Figure 45b shows the PL of Rx2, referenced to that of Rx1, or the path loss above free space, for the interlying area, which consists mostly of the forested area. As can be seen in Figure 45b, as frequency is increased, the attenuation rate of the PL lessens. This bending effect, is due to the contribution of higher order scattering on the mean power. At low frequencies, the dominate contributor to the mean power is from single scattering (forward scattering, represented by Foldy's theory, [37]). As frequency is increased, multiple scattering among leaves and branches, which decays at a lower rate than single scattering, begins to dominate the mean power, thus the bending observed in Figure 45b.

6.3.3 Frequency Correlation Analysis

Before beginning a frequency correlation analysis of the measured Lakehurst data, it is important to note that a post-processing procedure must first be performed, in which both a
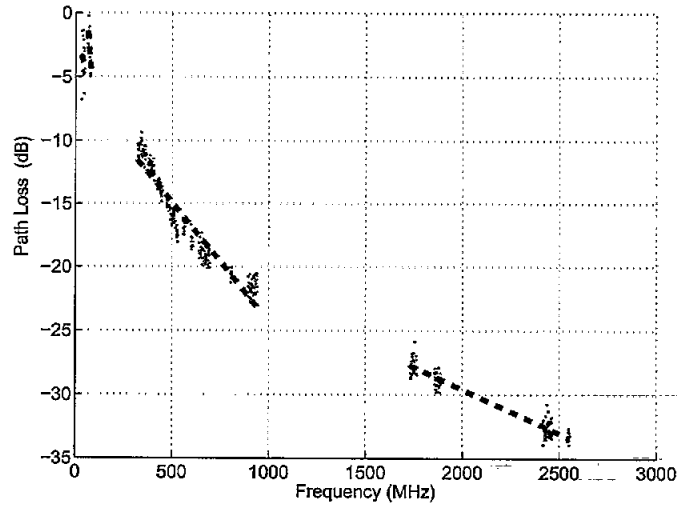
(a)

Figure 45: Path-loss through forest: (a) measurement scenario; (b) Path Loss above free space, Rx2 referenced to Rx1.

phase difference in the respective Tx and Rx PLLs, as well as a system frequency decorrelation, caused by phase noise in the error signal of the PLLs, must be accounted for.

In the wideband measurement system described, the frequencies of the phased lock loops (PLLs) of the two network analyzers are locked together but their phases are not. What this means, is that at the start of each frequency sweep, the relative phase of the two PLLs is unknown. This difference in absolute phase between the Tx and Rx VNAs is in the form of a linear phase shift, for each spatial sample, across the measured frequency band, similar to the phase shift that is caused by the propagation of the signal through free space. A way to circumvent this problem is to remove these linear phase shifts (constant group delays). In order to remove these delays, a frequency correlation is first performed on each spatial sample, and then an inverse discrete Fourier transform (IDFT) is applied to transform the data into the time domain. These phase delays are mapped into the time domain as time shifts. Recognizing that the free space time shift is constant for all spatial samples, the time domain impulses are now simply shifted to a common reference, and averaging is done over the spatial samples, in the time domain, and a discreet Fourier transform (DFT) performed, resulting in the corrected frequency correlation function.

In order to observe this time shift, we note that the actual received signal in the complex measurement environment can be represented by a form which includes the effects of the phase shift created by the different phases of the PLLs. Assuming no multi-path effects this form, for each spatial sample, is given by,

$$S_r(f) = S'(f) \; e^{j(2\pi f \tau_{fs} + \phi_{ch}(f) + \phi_{PLL}(f))}, \tag{40}$$

where $S'(f)$ is a complex amplitude function, τ_{fs} represents the free space propagation delay, $\phi_{ch}(f)$ represents the non-linear phase characteristics of the channel (as well as phase noise caused by the PLLs, which will be discussed later in this section) and $\phi_{PLL}(f)$ represents the phase shift caused by the relative phase differences of the PLLs of the VNAs. Noting

63

that $\phi_{PLL}(f)$ is a linear function of frequency, calculating the frequency correlation function of (40), Fourier transforming the resulting function, and applying the shifting theorem of Fourier transforms, gives the following form of the frequency correlation function in the time domain,

$$\hat{F}_r(T) = \hat{F}'(T)\ \hat{F}_r(T - \tau_{fs} - \tau_{PLL}), \tag{41}$$

where τ_{PLL} represents the constant time shift, for each spatial sample in the measured data, caused by the phase differences of the PLLs. Note that in (41), $\hat{F}'(T)$ is a complex function which includes the effects of both $S'(f)$ and $\phi_{ch}(f)$ in (40).

This effect can be observed in the time domain plots in Figure 46a, for the upper HF-band measured (70 ± 8 MHz), which shows this time shift for overlapping spatial samples. In this figure, for measurements taken at site Rx2 (approximately 1.1 Km from the transmitter, see Figure 44), the raw frequency domain data was adjusted to remove the free space phase delay of 1.1 Km, a frequency correlation performed, and a IDFT applied to the resulting correlation function. The free space phase delay is removed to prevent aliasing in the time domain. For these measurements, the data is sampled in frequency increments of 1 MHz, thus the alias free range of the time domain data is 300 m. By normalizing the frequency data to this free space phase delay, this alias free range is localized around the receiver. If the delay spread (in distance) between the direct and multi-path signal components is less within this 300 m (a valid assumption over the distances involved), the transformed data can be assumed to be alias free.

In Figure 46a, the shift in the observed peaks of the traces in this graph correspond to the phase shift caused by the unknown relative phases of the PLLs It is now a simple matter to shift each peak to a common reference, shown for all spatial samples in Figure 46b, and average the spatial samples in the time domain, observed in Figure 46c. Thus the unwanted phase shift, in each spatial sample, is negated. An FFT is then performed giving the desired, corrected frequency correlation function, seen in Figure 46d.

An additional factor that must be accounted for, in order to generate an accurate frequency correlation function is an inherent system decorrelation, caused by phase noise in the error signal (output) of the PLLs. Ideally, if one were to connect the transmit and receive sections of the measurement system together, gather a data set, and perform a frequency correlation, one would see a perfectly correlated channel. In practice, due to this phase noise in the PLLs, the system transfer function would not show perfect frequency correlation. To account for this it is recognized that the channel and system frequency correlation functions are statistically independent from one another, and therefore the correlation function of the measured signal can be considered to be the multiplication of the correlation function of the system and that of the channel, or,

$$R_r(\Delta F) = R_{sys}(\Delta F)\ R_{ch}(\Delta F). \tag{42}$$

To correct for the system decorrelation then, a calibration data set is taken by connecting the transmit and receive sections together. Equation (42) is then applied, and the measured data set simply normalized by this calibration data set. Note that this calibration for the system decorrelation has been applied to data shown Figure 46 as well as all results which follow.

Three sets of data, each selected from HF (70 ± 8 MHz), VHF (493 ± 23 MHz), and S-band (1872 ± 16 MHz), respectively, are used for the frequency correlation analysis. All data in this section is collected from site Rx2. Figure 47 shows the frequency correlation
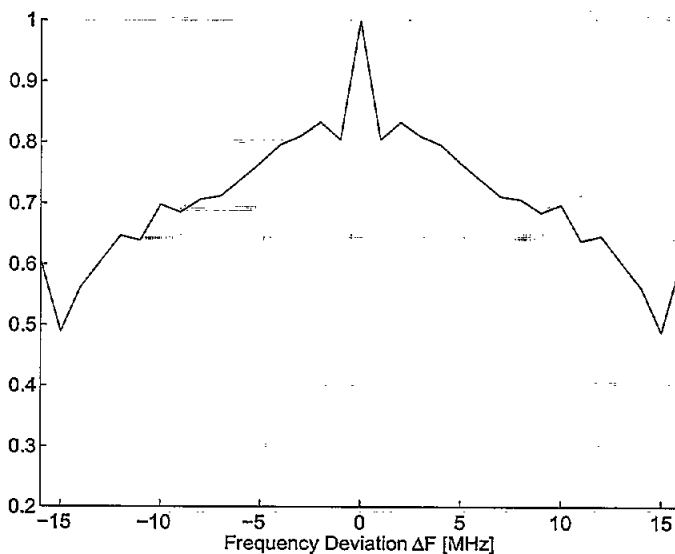
64
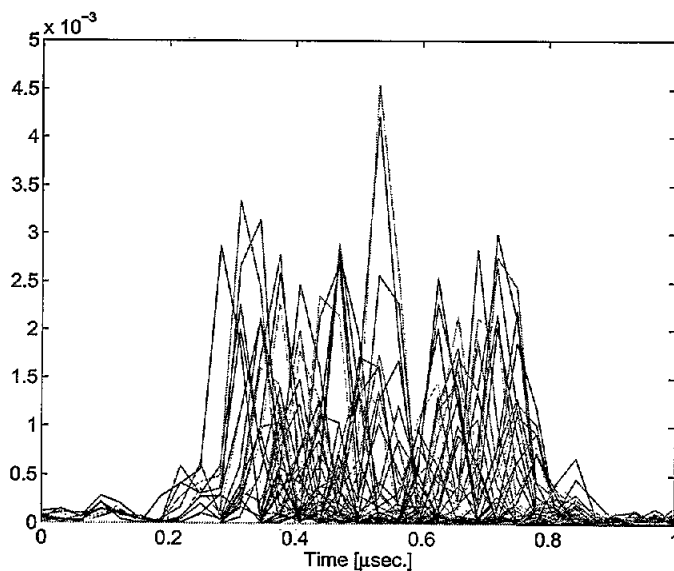
(a) Time domain response, HF band for 100 spatial samples, before correction for PLL phase shift.
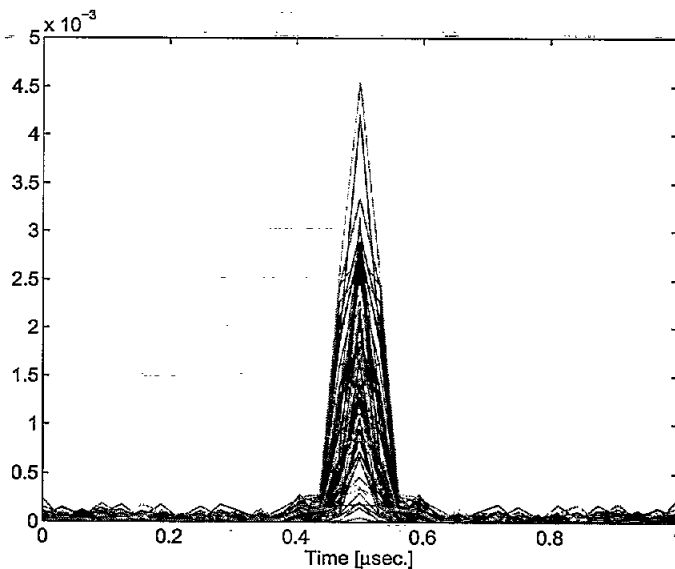
(b) Time domain response, HF band for 100 spatial samples, after correction for PLL phase shift.
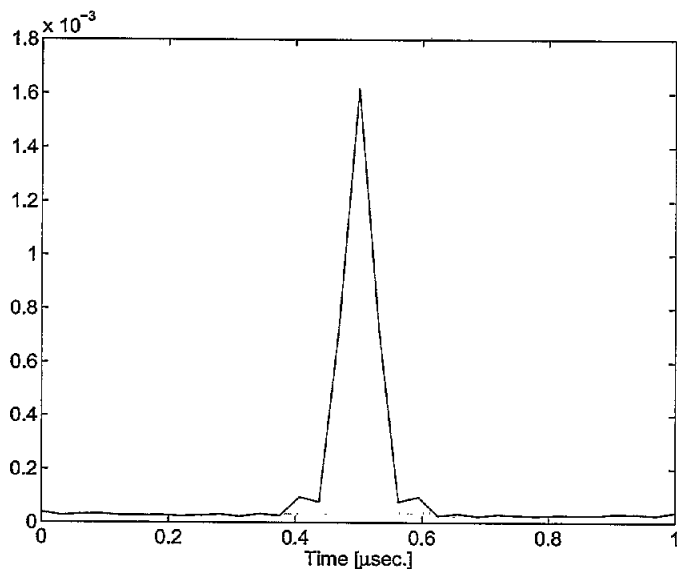
(c) Averaged (corrected) time domain response, HF band.

(d) Frequency correlation function, HF band.

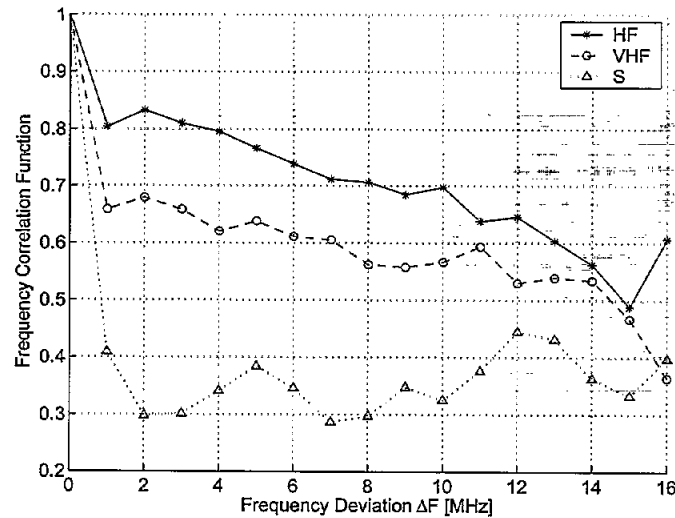Figure 46: Frequency Correlation Analysis, HF (70± 8 MHz) band.

Figure 47: A comparison of the frequency correlation functions for HF, VHF, and S-bands

functions for the three bands, overlapped for comparison. As can be observed in this plot there is a narrowing of the frequency correlation bandwidth for increased frequency. This is expected, as the dimensions of scatterers in the propagation environment (tree trunks, branches, twigs, leaves, short vegetation) become electrically larger, the random scattered field dominates, and decorrelates the received signal.

6.4   Conclusions

In this section of a novel, ultra wideband measurement system, for communications channel characterization was presented. The system is based on the application of two VNAs, one as a transmitter and one as a receiver, and who's frequency sweeps are synchronized by two RbAC atomic clocks. These clocks also provide an extremely stable frequency reference for the VNAs. The use of the VNAs and their ability to perform swept frequency measurements, with a narrowband IF filter allows for long distance, high sensitivity propagation measurements. For an IF bandwidth setting on the receiver NWA of 3 KHz, (it can be set as low as 3 Hz), and assuming a transmitter power of 10 W, the maximum measurable loss of the system, from 30 MHz to 3 GHz, was shown to exceed 115 dB.

This coherent system allows for measuring the attenuation and phase characteristics of the medium and studying temporal and frequency decorrelations. In order to demonstrate some of these capabilities, data was presented and analyzed from a measurements campaign at the Lakehurst Naval Air Station, in Lakehurst, New Jersey. It was shown that the slope of the attenuation of the mean power, caused by a forested area, tended to decrease with increased frequency, as multiple scattering effects within the forest medium began to dominate the path loss. Also frequency correlation analysis of the measured data was given. To perform this analysis, it was shown that a phase shift, caused by the phase difference in the independent PLLs in the system, must be accounted for, and a method was presented to correct for this shift. After also correcting for the inherent system decorrelation, caused by phase noise in the PLL error signal, frequency correlation data for three different sub-bands was presented, for a forested area at the Lakehurst base. It was shown that for higher frequency bands, the signal decorrelated at a faster rate, in frequency, as expected, due to

the increased effect of multipath on the received signal, as the forest components become electrically larger.

References

[1] K. Sarabandi and T.B.A. Senior, "Low-frequency Scattering from Cylindrical Structures at Oblique Incidence," *IEEE Trans. on Geoscience and Remote Sensing*, vol. 28, no. 5, pp. 879–885, 1990.

[2] I. Koh and K. Sarabandi, "Polarimetric Channel Characterization of Foliage for Performance Assessment of GPS Receivers Under Tree Canopies," *Submitted for publication in IEEE Trans. Antennas Propagat.*, 2002.

[3] A.D. Yaghjian, "Electric Dyadic Green's Functions in the Source Region," *Proceedings of the IEEE*, vol. 68, no. 2, pp. 248–263, 1980.

[4] D.E. Livesay and K. Chen, "Electromagnetic Fields Induced Inside Arbitrary Shaped Biological Bodies," *IEEE Trans. on Microwave Theory and Techniques*, vol. 22, no. 12, December 1974.

[5] G. T. Ruck, *Radar Cross Section Handbook, Volume 1*, Plenum Press, New York, 1970.

[6] K. Sarabandi M. D. Casciato and I. Koh, "Efficient Calculation of the Field of a Dipole Radiating Above an Impedance Surface," *Accepted for publication in IEEE Trans. Antennas Propagat.*

[7] R. Coifman V. Rokhlin and S. Wandzura, "The Fast Multipole Method for the Wave Equation:A Pedestrian Prescription," *IEEE Antennas and Propagation Magazine*, vol. 35, no. 3, pp. 7–12, June 1993.

[8] E. Bleszynski M. Bleszynski and T. Jaroszewicz, "AIM: Adaptive integral method for solving large-scale electromagnetic scattering and radiation problems," *Radio Sci.*, vol. 31, no. 5, pp. 1225–1251, September - October 1996.

[9] N. Geng A. Sullivan and L. Carin, "Fast Multipole Method for Scattering form an Arbitrary PEC Target Above or Buried in a Lossy Half Space," *IEEE Trans. Antennas Propagat.*, vol. 49, no. 5, pp. 740–748, May 2001.

[10] M. Abramowitz and I. A. Stegun, *Handbook of mathematical functions with formulas, graphs, and mathematical tables*, Wiley, New York, 1972.

[11] C. A. Balanis, *Antenna Theory: Analysis and Design*, Harper & Row, New York, 1982.

[12] J. R. Wait, *Electromagnetic Waves in Stratified Media*, IEEE Press, New York, 1996.

[13] Y. Okumura, E. Ohmori, T. Kawano, and K. Fukuda, "Field Strength and its Variability in VHF and UHF Land Mobile Service," *Rev. Elec. Comm. Lab*, vol. 16, pp. 825, September-October 1968.

[14] N. C. Rogers, A. Seville, J. Richter, D. Ndzi, N. Savage, R.F.S. Caldeirinha, A. K. Shukla, M. O. Al-Nuaimi, K. Craig, E. Vilar, and J. Austin, "A Generic Model of 1-60 GHz Radio Propagation through Vegetation-Final Report," Tech. Rep., Document produced by QinetiQ for the UK Radiocommunications Agency, May, 2002.

[15] A. G. Longley and P. L. Rice, "Prediction of Tropospheric Radio Transmission Loss Over Irregular Terrain, A Computer Method - 1968," Tech. Rep. ERL79-ITS67, ESSA Research Laboratories, Washington, D.C., 1968, US Government Printing Office.

[16] K. Sarabandi and I. Koh, "An Overview of Physics-Based Wave Propagation in Forested Environment," *International Workshop on Wave Propagation, Scattering and Emission (WPSE03): Theory, Experiments, Numerical Simulation and Inversion,* June 1-4, Shanhai, China (invited) 2003.

[17] F. Wang, I. Koh, and K. Sarabandi, "Theory and Measurements of Millimeter-wave Propagation Through Foliage," *Proceedings of the IEEE AP-S Symposium,* June 22-27,Columbus, OH 2003.

[18] F. Aryanfar, I. Koh, and K. Sarabandi, "Physics Based Ray-tracing Propagation Model for Sub-urban Areas," *Proceedings of the IEEE AP-S Symposium,* June 22-27, Columbus, OH 2003.

[19] L. Pierce and K Sarabandi, "Parallelized Physics-Based Foliage Wave Propagation Model," *Proc. The 2003 EMCC Annual Meeting,* May 20-22, Virginia 2003.

[20] K. Sarabandi and I. Koh, "Effect of Canopy-air Interface Roughness on HF-UHF Propagation in Forest," *IEEE Trans. Antennas Propagat.,* vol. 50, no. 1, pp. 111–122, January 2002.

[21] K. Sarabandi and I. Koh, "A Complete Physics-based Channel Parameter Simulation for Wave Propagation in a Forest Environment," *IEEE Trans. Antennas Propagat.,* vol. 49, no. 2, pp. 260–271, February 2001.

[22] I. Koh, F. Wang, and K. Sarabandi, "Estimation of Coherent Field Attenuation Through Dense Foliage Including Multiple Scattering," *Accepted for publication in IEEE Trans. Geosci. Remote Sensing.*

[23] M. D. Casciato, S. Oveisgharan, and K. Sarabandi, "Radio Wave Propagation in the Presence of a Coastline," *Radio Science,* vol. 38, no. 5, October 2003.

[24] M. D. Casciato and K. Sarabandi, "High Frequency Radio Wave Diffraction from Singly Curved Convex Surfaces - A Heuristic Approach," *IEE Proceedings-Microwave, Antennas and Propagat.,* vol. 151, no. 1, pp. 43–53, February 2004.

[25] N. C. Currie, F. B. Dyer, and E. E. Martin, "Millimeter Foliage Penetration Measurements ," 1976.

[26] F. K. Schwering, E. J. Violette, and R. H. Espeland, "Millimeter-Wave Propagation in Vegetation: Experiments and Theory ," *IEEE Transactions on Geoscience and Remote Sensing,* vol. 26, no. 3, pp. 355–367, May 1988.

[27] A. Y. Nashashibi, K. Sarabandi, S. Oveisgharan, M. C. Dobson, W. Walker, and E. Burke, "Millimeter-Wave Measurements of Foliage Attenuation and Ground Reflectivity of Tree Stands at Nadir Incidence," *accepted for publication in IEEE Trans. Antennas and Propagat.,* vol. 52, no. 4, Apr. 2004.

[28] R. J. C. Bultitude, P. Melancon, H. Zaghloul, G. Morrison, and M. Prokki, "A Comparison of Indoor Radio Propagation Characteristics at 910 MHz and 1.75 GHz," *IEEE J. Sel. Areas Commun.*, vol. 7, no. 1, pp. 20–30, January 1989.

[29] J. G. O. Moss, M. P. Fitton, A. M. Street, K. M. Brown, C. C. Constantinou, and D. J. Edwards, "Spatio-Temporal Variability Analysis of the Wideband Microcellular Environment," pp. 293–297, 1998.

[30] J. Liu, C. P. Wei, D. Chang, C. Chang, and C. Cheng, "Estimating the RF Attenuation Rate Via Roadside Trees with Extraction Techniques," *Microwave and optical technology letters, John Wiley & Sons, Inc.*, vol. 30, no. 4, pp. 242–246, Aug. 2001.

[31] C. L. Rino and J. Owen, "Wideband Propagation Measurements in Forested Media," Tech. Rep. under contract DAAD-07-85-C-K569, SRI International (project 8899), submitted to U.S. Army Communications-Electronics Command (CECOM), Fort Monmouth, NJ, Aug. 1988.

[32] S. J. Howard and K. Pahlavan, "Measurement and Analysis of the Indoor Radio Channel in the Frequency Domain," *IEEE Transact. Instrumentation and Measurement*, vol. 39, no. 5, pp. 751–755, October 1990.

[33] H. Zaghloul, G. Morrison, and M. Fattouche, "Frequency Response and Path Loss Measurements of Indoor Channel," *Electron. Lett.*, vol. 27, no. 12, pp. 1021–1022, Oct. 1991.

[34] A. M. Street, J. G. O. Moss, and D. J. Edwards, "Outdoor-indoor Wideband Channel Study for Third Generation Communication Systems," Mar. 1999.

[35] A. M. Street, L. Lukama, and D. J. Edwards, "Use of VNAs for Wideband Propagation Measurements," *IEE Proc.-Commun.*, vol. 148, no. 6, Dec. 2001.

[36] PRS10, "PRS10 Rubidium Frequency Standard," Tech. Rep., Stanford Reasearch Systems.

[37] L. L. Foldy, "The Multiple Scattering of Waves," *Phys. Rev.*, vol. 67, pp. 107–119, 1945.